

THESIS

USING WAVEFORM MODELING OF SEISMIC ANISOTROPY TO UNDERSTAND THE PROCESS OF  
PROTEROZOIC LITHOSPHERIC ASSEMBLY

Submitted by

Melinda A Solomon

Department of Geosciences

In partial fulfillment of the requirements

For the Degree of Master of Science

Colorado State University

Fort Collins, Colorado

Spring 2013

Master's Committee:

Advisor: Derek Schutt

Dennis Harry

Judy Hannah

Jay Breidt

## ABSTRACT

### USING WAVEFORM MODELING OF SEISMIC ANISOTROPY TO UNDERSTAND THE PROCESS OF PROTEROZOIC LITHOSPHERIC ASSEMBLY

In this study, SKS data from two long-standing broadband seismic stations located along the Proterozoic Trans Hudson Orogen is analyzed for the effects of complex anisotropy. The Trans Hudson Orogen is the lasting expression of collisional events that brought together Archean continental fragments to form the cratonic core of the North American continent. Split SKS waveforms observed at two GSN stations, FFC located on the Sask craton near Flin Flon, Manitoba, and RSSD located on the eastern margin of the Wyoming craton in the Black Hills of South Dakota, are analyzed for anisotropic layering of varying complexity. At FFC we find that a model with two flat layers of anisotropy is better able to explain the data than the simple model of one flat layer. A top layer shows anisotropy perpendicular to the convergence direction of the Trans Hudson Orogen that is similar to observations of anisotropy today at convergent margins, and is attributed to lithospheric deformation during convergence. RSSD shows more complex splitting that we interpret as sub-wavelength scale anisotropic heterogeneity resulting from convergence driven fragmentation of the pre-existing lithosphere into small,  $< \sim 40$  km pieces. Previous studies show more coherent anisotropy to the east and west of RSSD, suggesting that anisotropic heterogeneity here is related to the convergence, and may be a longstanding feature of tectonic boundaries.

## ACKNOWLEDGEMENTS

I'd like to express my sincere gratitude to Dr. Derek Schutt for his guidance and supervision in the completion of this project. His vast experience and technical input were vital to progression and completion of my research at Colorado State University. I'd also like to thank my committee members Dr. Dennis Harry, Dr. Jay Breidt, and Dr. Judy Hannah for their time, help, and input along the way. I'd also like to thank Dr. Huiayu Yuan (now at Berkeley) for allowing us to use and modify his programs, and for providing assistance throughout the project. Thank you also to Robin McGee and Randy Major for their help with my computing needs. Lastly, I'd like to thank the faculty and graduate students in the Geosciences department for providing me with the knowledge necessary to complete my degree. Funding for this research was provided by a graduate research assistantship working under Dr. Derek Schutt, and a graduate teaching assistantship from Colorado State University.

# TABLE OF CONTENTS

	<u>Page</u>
ABSTRACT.....	II
ACKNOWLEDGMENTS.....	III
LIST OF TABLES.....	VII
LIST OF FIGURES.....	VIII
CHAPTER 1 INTRODUCTION.....	1
1.1 ORGANIZATION OF THESIS.....	1
1.2 SHEAR WAVE SPLITTING AND MANTLE ANISOTROPY.....	1
1.2.1 INTRODUCTION.....	1
1.2.2 MAKING THE MEASUREMENT.....	2
1.2.3 ANISOTROPY IN THE MANTLE.....	5
1.2.4 LIMITATIONS OF COMMON METHODS.....	7
1.3 MOTIVATION.....	10
CHAPTER 2 USING WAVEFORM MODELING OF SEISMIC ANISOTROPY TO UNDERSTAND THE PROCESS OF PROTEROZOIC LITHOSPHERIC ASSEMBLY.....	11
2.1 SUMMARY.....	11
2.2 INTRODUCTION.....	12
2.2.1 TECTONIC SETTING.....	12
2.2.2 MANTLE ANISOTROPY.....	13
2.2.3 A MULTIPLE LAYER APPROACH.....	15
2.3 DATA AND METHODS.....	17

2.3.1 SHEAR WAVE DATA SELECTION .....	17
2.3.2 SILVER AND CHAN METHOD ANALYSIS .....	21
2.3.3 MODEL PARAMETERIZATIONS .....	21
2.3.4 SEARCHING PARAMETER SPACE .....	22
2.3.5 MODEL INFERENCE .....	23
2.3.6 SYNTHETIC TESTING.....	24
2.4 RESULTS .....	25
2.4.1 SILVER AND CHAN METHOD RESULTS.....	25
2.4.2 FFC.....	26
2.4.2.1 Weighting events by back azimuth .....	26
2.4.2.2 Model inference and ranking.....	31
2.4.2.3 Synthetic testing .....	35
2.4.2.4 Summary of results at FFC .....	41
2.4.3 RSSD .....	42
2.4.3.1 Best fitting solutions .....	42
2.4.3.2 Bootstrap analysis.....	46
2.4.3.3 Synthetic testing .....	50
2.4.3.4 Summary of results at RSSD.....	53
2.5 DISCUSSION.....	53
2.5.1 FFC.....	53
2.5.2 RSSD .....	57
2.6 CONCLUSIONS.....	59
CHAPTER 3 PROCESSING AND RECOMMENDATIONS.....	62
3.1 OVERVIEW OF PROCESSING .....	62

3.1.1 DATA AQUISION .....	62
3.1.2 QUALITY CONTROL AND DATA FORMATTING .....	63
3.1.3 RUNNING RAYSUM .....	66
3.1.4 SYNTHETIC SEISMOGRAMS.....	69
3.1.5 PROCESSING LIMITATIONS AND PATHS FORWARD .....	71
3.2 RECOMMENDATIONS FOR ONGOING WORK.....	72
LITERATURE CITED .....	74
APPENDICIES .....	81

LIST OF TABLES

	<u>Page</u>
1. EVENT TABLE FOR FFC AND RSSD .....	18
2. MODEL RESULTS FOR UN-WEIGHTED FFC DATA SET.....	28
3. MODEL RESULTS FOR WEIGHTED FFC DATA SET .....	29
4. MODEL RESULTS FOR RSSD DATA SET .....	43
5. BEST FITTING SOLUTIONS FOR RSSD_SD_A.....	50
6. BEST FITTING SOLUTIONS FOR RSSD_SD_C .....	51

LIST OF FIGURES

	<u>Page</u>
1. SHEAR WAVE SPLITTING IN AN ANISOTROPIC MEDIUM .....	2
2. CARTOON SHOWING THE PATH OF AN SKS RAY.....	3
3. EFFECTS OF ANISOTROPY ON RADIAL AND TRANSVERSE COMPONENTS.....	5
4. EFFECTS OF COMPLEX ANISOTROPY ON ASP.....	8
5. PRECAMBRIAN BASEMENT OF NORTH AMERICAN CONTINENT .....	13
6. CROSS SECTION THROUGH SASK CRATON.....	14
7. EVENT LOCATION MAPS FOR FFC AND RSSD .....	19
8. SKS WAVEFORMS FOR FFC AND RSSD .....	20
9. CARTOON OF 4 MODEL PARAMETERIZATIONS.....	22
10. SILVER AND CHAN METHOD RESULTS FOR FFC AND RSSD.....	26
11. COMPARISON OF BOOTSTRAP RESULTS FOR FFC UN-WEIGHTED AND WEIGHTED DATA SETS TO PDF MARGINALS.....	30
12. 1-D PPF MARGINALS FOR WEIGHTED FFC DATA SET.....	32
13. 2-D PPF AMRGINALS FOR WEIGHTED FFC DATA SET.....	33
14. F-TEST RESULTS FOR FFC.....	35
15. 1-D BOOTSTRAP DISTRIBUTIONS FOR FFC_SD_A .....	37
16. 2-D BOOTSTRAP DISTRIBUTIONS FOR FFC_SD_A .....	38
17. 1-D BOOTSTRAP DEISTRIBUTIONS FOR FFC_SD_D .....	40

18. 2-D BOOTSTRAP DEISTRIBUTIONS FOR FFC_SD_D .....	41
19. 1-D PPF MARGINALS RSSD DATA SET.....	44
20. 2-D PPF MARGINALS RSSD DATA SET.....	45
21. F-TEST RESULTS FOR RSSD .....	46
22. 1-D BOOTSTRAP DISTRIBUTIONS FOR RSSD DATA SET .....	47
23. 2-D BOOTSTRAP DISTRIBUTIONS FOR RSSD DATA SET .....	48
24. 2-D BOOTSTRAP DISTRIBUTIONS FOR RSSSD DATA SET MODEL C SOLUTIONS .....	49
25. MODEL A AND C 2-D BOOTSTRAP DISTRIBUTIONS FOR RSSD_SD_A AND RSSD_SD_C.....	52
26. INTERPRETATION OF ANISOTROPY AT FFC .....	54
27. JOINT SURFACE WAVE-SKS INVERSION RESULTS.....	56
28. SWS RESULTS FROM SILVER AND CHAN .....	58
29. BASIC PROCESSING STREAM.....	63
30. QUALITY CONTROL PROCESSING STREAM.....	64
31. EXAMPLE WAVEFORM THAT WOULD FAIL VISUAL INSPECTION.....	65
32. DEMONSTRATION OF AUTOMATIC WINDOW SELECTION .....	66
33. PROCESSING STREAM FOR RAYSUM_SKS.....	68
34. PROCESSING STREAM FOR GENERATING SYNTHETIC SEISMOGRAMS.....	70
35. ADDING NOISE TO SYNTHETICS .....	71

# Chapter 1

## INTRODUCTION

### 1.1 Organization of thesis

The data, method, analyses, and research findings presented in Chapter 2 of this thesis are organized into a technical paper to be presented to a professional journal (the Journal of Geophysical Research) and therefore do not follow the layout of a classical thesis. As such, this chapter (**Chapter 1**) is offered to present background information and motivation for this research, and **Chapter 3** offers a processing summary along with recommendations for future researchers.

### 1.2 Shear Wave Splitting and Mantle Anisotropy

#### 1.2.1 Introduction

The upper roughly 200 km part of the mantle is thought to accommodate strain through the dislocation creep deformation mechanism [e.g. *Jung and Karato, 2001*]. Under these conditions, olivine, and to a lesser extent orthopyroxene, crystalline grains tend to line up in a preferred direction that is a sometimes complicated function of the strain history of that region of the mantle. This mineral alignment is often called crystalline preferred orientation or lattice preferred orientation and produces an elasticity tensor that is anisotropic. Seismic waves propagating through this material experience different velocities as a function of their direction of propagation and polarization. When shear waves encounter anisotropic material, they split into two orthogonally polarized components with separate “slow” and “fast” propagation velocities (**figure 1**). This phenomenon is called shear wave birefringence or shear wave splitting (SWS). This process allows seismologists to investigate deformation at depths inaccessible to direct observation. Researchers have been using this method to provide important constraints on mantle

structure and dynamics for over three decades [e.g. *Silver and Chan*, 1988; *Vinnik et al.*, 1992; *Savage and Silver*, 1993; *Ozalaybey and Savage*, 1995; *Savage and Sheehan*, 2000; *Schutt and Humphreys*, 2001; *Fouch and Rondenay*, 2006], particularly in continental interiors, where it can help address important issues that remain unresolved, including assessing the nature of a mechanical asthenosphere (if it is even present) that concentrates shear [*Schutt and Humphreys*, 2001], and the role of the lithospheric mantle in orogenic deformation.

### 1.2.2 Making the measurement

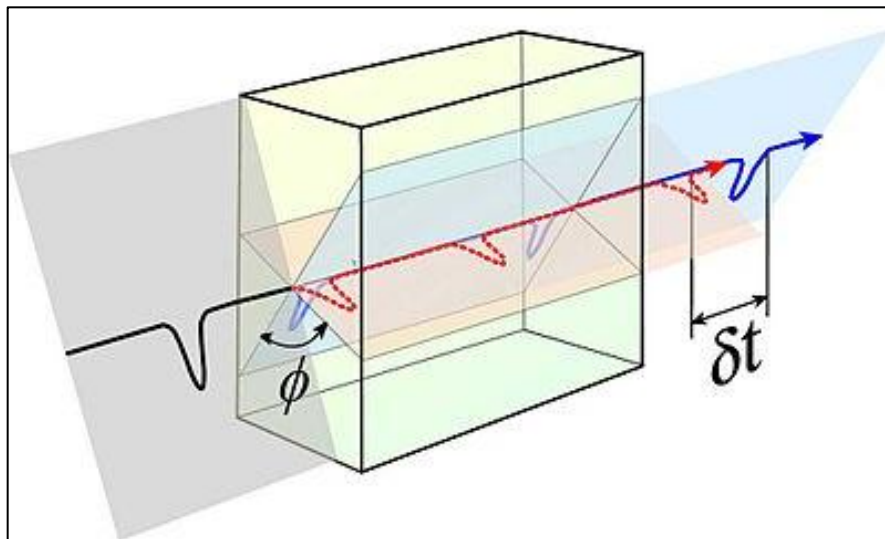


**Figure 1.** Shear wave splitting in an anisotropic medium from E. Garnero [unpublished data, 2012] available from (<http://garnero.asu.edu/>). Upon entering an anisotropic medium (yellow box), a shear wave initially polarized in the radial plane (grey plane) will be split into two components. The fast component (blue) is polarized in the seismically fast direction of the medium, and the slow component (red) is polarized orthogonal to the fast component. The apparent splitting parameters of  $\delta t$  and  $\Phi$ , which describe the delay time between the components and the polarization of the fast velocity axis, respectively, are searched for in order to describe the anisotropic medium.

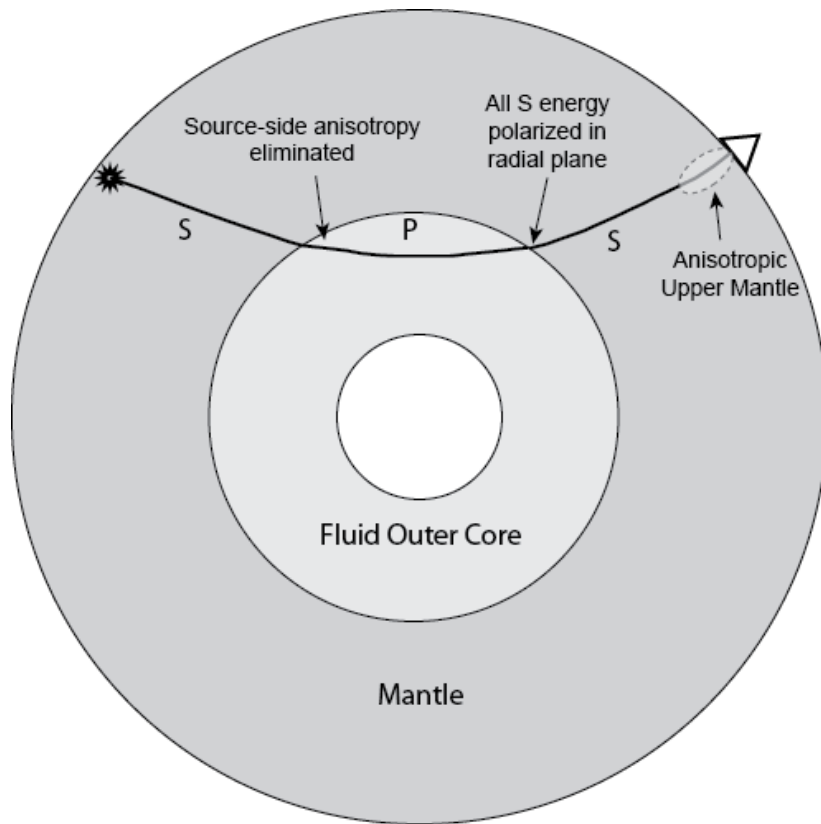


**Figure 2.** Cartoon showing the path of an SKS ray. Shear wave energy cannot propagate through a fluid. Therefore when the SKS ray encounters the core-mantle-boundary, it is converted from a shear wave to a compressional wave. All effects of source-side anisotropy are removed by this conversion. Upon exiting the outer-core, it is converted back into a shear wave that is polarized in the radial plane.

When a shear wave is split into two orthogonally polarized components, the splitting can be measured via two parameters: the delay time ( $\delta t$ ) between the two components, and the “fast axis”—the polarization direction of the fast component. The delay time between the two components is an effect of both the degree of alignment and the thickness of the layer [Silver, 1996]. The polarization of the fast component generally aligns with the direction of maximum extension or maximum shear, but this relationship can be altered in the presence of specific temperature, pressure, and water contents [Ribe, 1992; Zang and Karato, 1995; Jung and Karato, 2001; Kaminiski, 2002]. When there is only one layer of anisotropy, these parameters directly relate to the anisotropic elasticity tensor and the flow fabric through which the wave has travelled. However, if

there are multiple layers of anisotropy, the shear wave gets split multiple times, and the observed splitting parameters will vary with the direction of propagation of the shear wave. For this reason, the splitting parameters are often called apparent splitting parameters (ASP) to indicate they may vary as a function of seismic wave propagation path to a given station. The process of deducing the meaning of ASP is simplified when the initial polarization of the shear wave, before it is affected by anisotropy, is known. A particularly useful phase is SKS (**figure 2**). Typically, the effects of anisotropy are integrated over the whole ray path, but as the SKS pulse travels through the outer core it is converted to a P wave, and exits the outer core as an S wave polarized entirely in the radial plane, which is defined as the plane containing both the source (earthquake) and receiver (seismometer). This process removes any effects of source side anisotropy (**figure 2**). If no anisotropy is encountered, all SKS energy should be in the radial plane. However if the SKS has been split, energy will be present in the transverse plane, which is the plane orthogonal to the radial plane. The goal of common SWS methods is to find the set of ASP that can explain the energy observed on the transverse component of broadband seismic data via a process that generally involves searching for events that contain a SKS arrival, rotating the N-S and E-W seismogram components into radial and transverse components, filtering out events with a low signal to noise ratio, selecting a time window for analysis, and examination of resulting diagnostics.

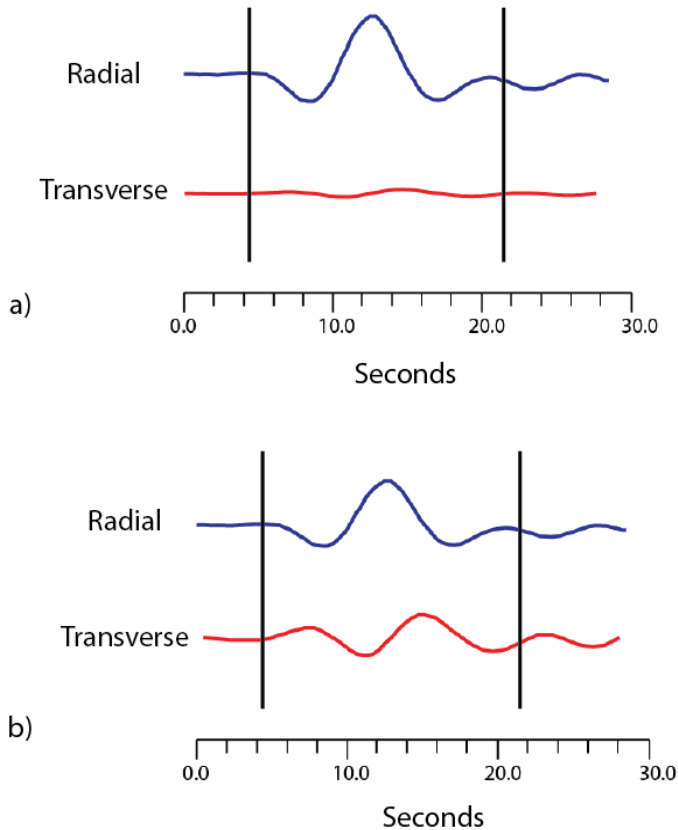


**Figure 3.** Schematic diagram showing the effects of anisotropy on radial and transverse components. For a shear wave that has not undergone splitting (a), all energy is on the radial component. In the presence of anisotropy (b), energy is split between the radial and transverse components.

### 1.2.3 Anisotropy in the mantle

Because the effects of anisotropy are integrated over the whole ray path, or at least the receiver-side leg in the case of an SKS phase, an understanding of where anisotropy occurs in the mantle is integral in relating SWS observations to mantle deformation. Anisotropy exists within the mantle in certain regions where pressure, temperature, and fluid conditions allow strain to be accommodated by the dislocation creep deformation mechanism [Karato *et al.*, 2007]. These conditions are found in the mantle lithosphere, the upper-most asthenosphere, and the D'' layer that sits above the outer core. Below the uppermost asthenosphere, and above D'', strain is

accommodated by diffusion creep, and anisotropic fabric is not developed. Although recent advances in mineral physics have greatly increased our understanding of how anisotropy develops, the exact temperature, pressure, and other characteristics that define the transition from dislocation to diffusion creep are not definitively known. One theory is that the seismically observable Lehmann discontinuity (at ~220 kilometers depth) marks the transition from dislocation to diffusion creep, and thus marks the bottom of potentially anisotropic material in the upper mantle [Karato, 1992; Gaherty and Jordan, 1995].

Beneath ocean basins, shear in the upper-most asthenosphere due to ongoing Couette-type flow of the asthenosphere induced by lithospheric motion is the most likely cause of anisotropy [e.g. Long and Silver, 2009]. In continental regions, characterizing observed anisotropy is not so simple. A mechanical asthenosphere that concentrates shear may give rise to anisotropy similar to that observed in ocean basins [Vinnik *et al.*, 1992]. But unlike ocean basins, this lithospheric mantle beneath the continents is old, cold, and thick and may contain anisotropic fabrics that were formed during large-scale tectonic events and then frozen-in during subsequent cooling [Silver, 1996]. Numerous SWS observations from continental regions have been published that support both end member cases.

When observations of anisotropy are made, one also must consider the effects of the crust. Preferentially aligned cracks in the upper crust [Crampin and Lovell, 1991], and alignment of minerals in the lower crust, can also cause anisotropy [e.g. Mainprice and Nicolas, 1989]. However, measurements of crustal anisotropy suggest the total split time contribution to an SKS phase from the crust is minimal [e.g. Iidaka and Niu, 2001], and hence the crustal contribution to anisotropy is assumed to be negligible in this study.

#### ***1.2.4 Limitations of common methods***

Common SWS approaches have limitations and contain simplifications that can strongly bias interpretation. First, as discussed above, the effects of anisotropy are integrated over the ray path, and therefore SWS suffers from issues of poor vertical resolution. While constraints from mineral physics dictate that most anisotropy is found in the uppermost asthenosphere or within the mantle lithosphere, it is not possible to determine exactly where observed anisotropy is encountered along the ray path. Secondly, common methods contain the assumption that only a single flat layer of anisotropy is present. Under those conditions, ASP can be directly related to anisotropic geometry. But, as mentioned above, when anisotropy is more complex (e.g. multiple and/or dipping layers), ASP display variations that are dependent on the back azimuth and incidence angle of the incoming ray, and cannot be directly related to the geometry of either layer (**figure 4**). Numerous studies have shown that ASP variations can be used to diagnose complexity, but common methods are incapable of accurately describing it.

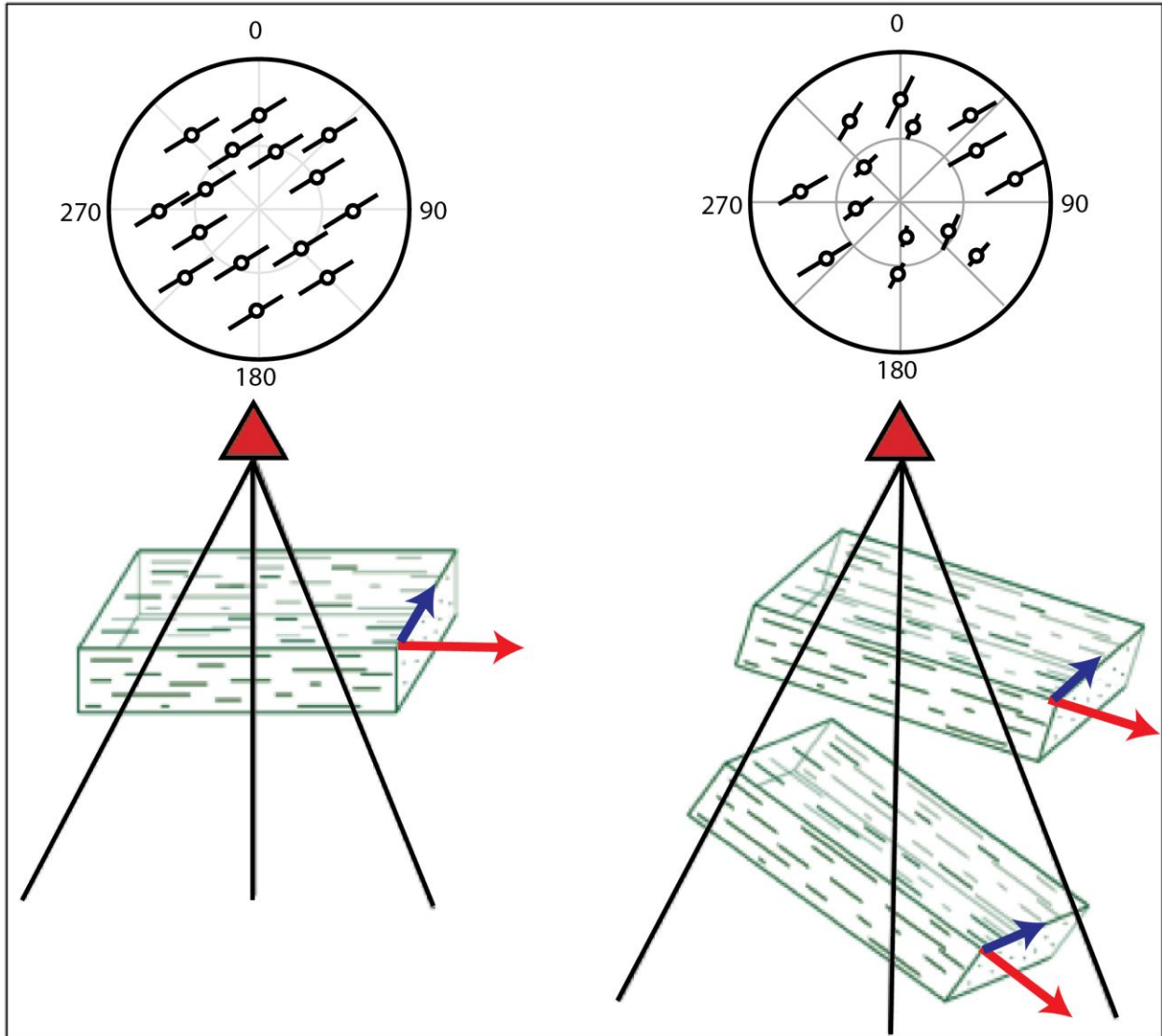


**Figure 4.** Effect of complex anisotropy on ASP. Theoretical ASP solutions are shown as black lines in the circles.  $\phi$  is shown by the orientation of the black line, and  $\delta t$  is proportional to its length. The back azimuth of the incident ray is shown by the line's position along the perimeter of the circle, and the inclination angle is shown by its distance from the center. Red arrows show the orientation of the fast velocity axis, and red arrows show the orientation of the slow velocity axis. In the presence of one flat layer of anisotropy (a), ASP from all back azimuths will be similar. In the presence of two or more layer (b), ASP will vary with back azimuth.

In ocean basins, and along continental margins, where the lithosphere is young and thin, the source of anisotropy is likely to be shear due to plate motion, with little or no contribution from the lithosphere. In this case, the single layer approximation is generally appropriate. But in continental interiors, where a cold thick lithosphere may contribute significantly to observed anisotropy,

complex structures likely exist [*Silver and Savage, 1994; Montagner et al., 2000; Silver and Long, 2010*]. Here the single layer approximation is not appropriate, and measurements of ASP cannot be directly interpreted. In the latter case, it is not yet known if or how much the lithosphere contributes to anisotropy, or whether or not active shear of the asthenosphere plays a role.

Other methods, particularly surface wave inversion, have identified vertically stratified anisotropic structures beneath continental interiors [e.g. *Yuan et al., 2011*], but the lateral resolution of surface waves is generally limited to ~400 km for regional studies and ~2000 km for global studies [*Montagner et al., 2000*]. Evidence suggests that anisotropic lateral heterogeneity may exist below the sensitivity level of surface waves [*Silver and Chan, 1991; Silver and Kaneshima, 1993*]. Because the lateral resolution of an SKS wave in the upper mantle is less than ~40 kilometers, SKS studies are more capable of resolving the small-scale structures possibly present in the sub-continental lithospheric mantle.

Important questions remain unresolved regarding mantle dynamics beneath continents, including whether lithospheric topography guides asthenospheric flow [*Fouch and Fischer, 2000*], and the role of the lithospheric mantle in orogenic deformation. Characterizing small-scale anisotropy can help address these issues, but a SWS method capable of going beyond diagnosing and moving toward fully describing complex anisotropy is required. In 2007, *Yuan et al.* developed a new method capable of discriminating between complex upper-mantle anisotropic velocity models to identify two dipping layers of anisotropy beneath Billings, Montana. That study found a lower layer that correlated with expected shear due to plate motion, and an upper layer that they attributed to frozen-in fabrics in the lithosphere.

### 1.3 Motivation

The motivation for this study was to expand on the method of *Yuan et al.* [2007] to investigate anisotropy beneath station FFC located near Flin Flon, Manitoba, and station RSSD located within the Black Hills of South Dakota. Both stations were chosen for their location along the Trans Hudson Orogen and their availability of data (over 10 years archived). Furthermore, previous seismic reflection, SWS, and tomographic inversion studies provided strong evidence for the existence of complex anisotropy at both locations, but fell short in describing its geometry [*Silver and Chan, 1991; White et al., 2003; Hajnal et al., 2005; Gorman et al., 2006; Hammer et al., 2011; Tian et al., 2011; Yuan et al., 2011*]. Thus a vital key in understanding the deformational history of the Trans Hudson Orogen was missing, and by using the method of *Yuan et al.*, [2007], this study seeks to fill that gap in knowledge by describing anisotropic fabrics locked in the lithosphere, as well as actively forming anisotropic fabrics within the asthenosphere.

## Chapter 2

### Using waveform modeling of seismic anisotropy to understand the process of Proterozoic lithospheric assembly

#### 2.1 Summary

In this study, SKS data from two long-standing broadband seismic stations located along the Proterozoic Trans Hudson Orogen is analyzed for the effects of complex anisotropy. The Trans Hudson Orogen is the lasting expression of collisional events that brought together Archean continental fragments to form the cratonic core of the North American continent. Split SKS waveforms observed at two GSN stations, FFC located on the Sask craton near Flin Flon, Manitoba, and RSSD located on the eastern margin of the Wyoming craton in the Black Hills of South Dakota, are analyzed for anisotropic layering of varying complexity. At FFC we find that a model with two flat layers of anisotropy is better able to explain the data than the simple model of one flat layer. A top layer shows anisotropy perpendicular to the convergence direction of the Trans Hudson Orogen that is similar to observations of anisotropy today at convergent margins, and is attributed to lithospheric deformation during convergence. RSSD shows more complex splitting that we interpret as sub-wavelength scale anisotropic heterogeneity resulting from convergence driven fragmentation of the pre-existing lithosphere into small,  $< \sim 40$  km pieces. Previous studies show more coherent anisotropy to the east and west of RSSD, suggesting that anisotropic heterogeneity here is related to the convergence, and may be a longstanding feature of tectonic boundaries.

## 2.2 Introduction

### 2.2.1 Tectonic Setting

The cratonic core of the North American continent was formed in the Paleoproterozoic (2.0-1.8 Ga) by the amalgamation of Archean continents and smaller continental fragments, and the resulting Trans-Hudson Orogen collisional belt is the lasting expression of these events (**figure 5**). An impressive amount of geologic and geophysical evidence has been collected from the Trans Hudson Orogen in the past three decades, providing an ideal opportunity for researchers today to investigate continent-forming collisional processes that occurred in the Precambrian. The Trans Hudson Orogen contains mostly reworked Archean crust with smaller remnants of juvenile volcanic belts preserved between Archean masses [*Whitmeyer and Karlstrom, 2007*]. It was during this time that the thick, buoyant, and compositionally depleted mantle lithosphere that underlies the cratonic core of North America was amalgamated, but the mechanism by which continental mantle lithosphere is accommodated by convergence remains poorly understood [*Pysklywec et al., 2010*]. Seismic imaging from the Canadian Lithoprobe project has provided a comprehensive understanding of the lithospheric structures associated with the Trans Hudson Orogen [*White et al., 2003; Hajnal et al., 2005; Gorman et al., 2006; Hammer et al., 2011; Tian et al., 2011*], and recent advances in surface wave tomography models have provided insights into the heterogeneous nature of anisotropic fabrics in the mantle beneath the Trans Hudson Orogen [*Yuan & Romanowicz 2010; Yuan et al., 2011*].

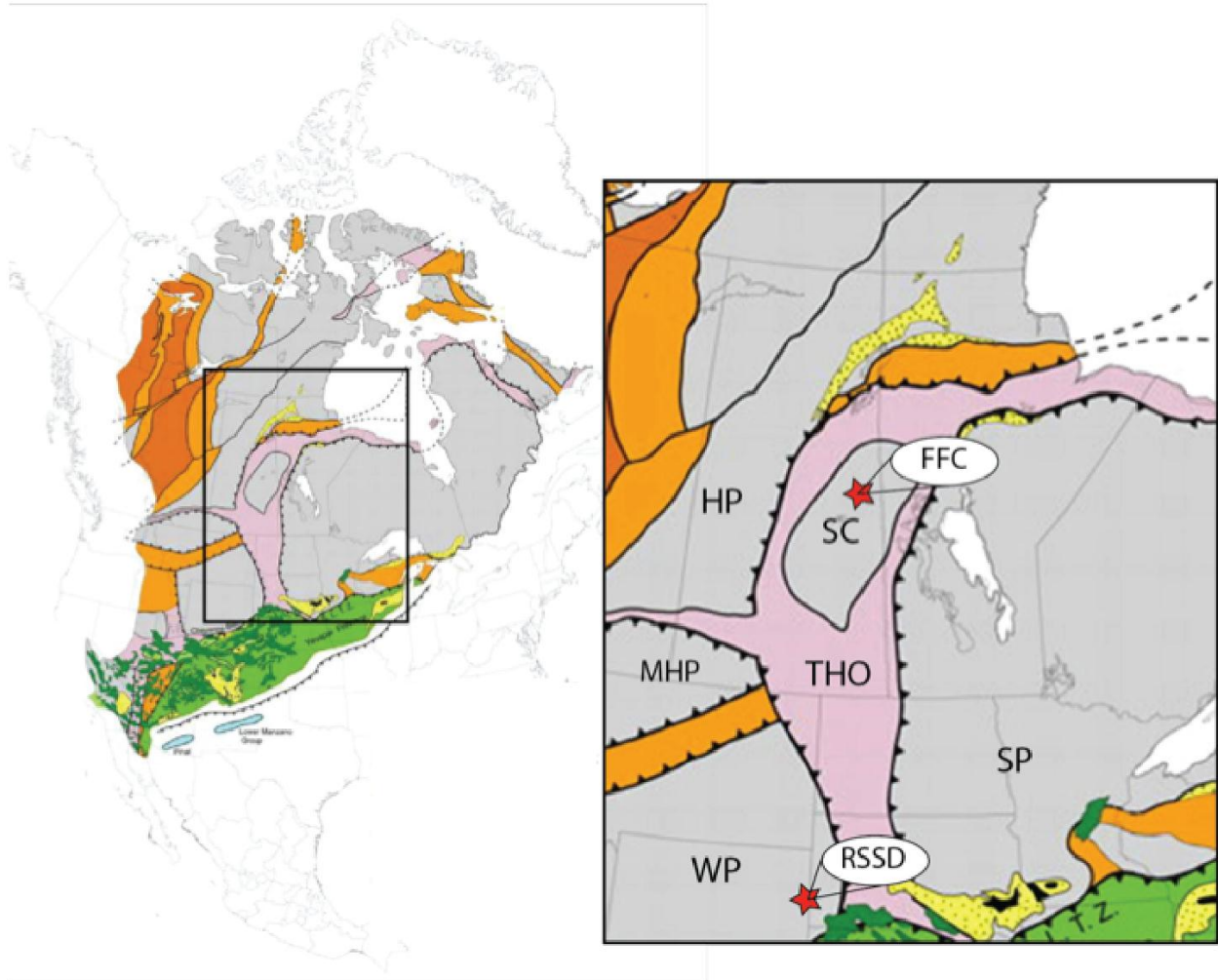


**Figure 5.** Precambrian basement of the North American continent showing major provinces and boundaries [Whitmeyer and Karlstrom, 2007]. Basement terranes shown are the Hearne Province (HP), Sask craton (SC), Trans Hudson Orogen (THO), Superior Province (SP), Medicine Hat Block (MHP), and Wyoming Province (WP). Seismometer locations for FFC and RSSD are marked by red triangles. FFC is located near Flin Flon, Canada, within the Proterozoic Trans Hudson Orogen on the Eastern edge of the Sask craton. RSSD is located on the Eastern margin of the Wyoming Province in close proximity to the Trans Hudson Orogen.

### 2.2.2 Mantle Anisotropy

One of the exciting findings of the Lithoprobe project was the identification of the intact Archean Sask craton trapped within the Trans Hudson Orogen (**figure 6**) [Hajnal et al, 2005], which requires that the mechanics of sub-continental lithospheric mantle interaction during collision is complex. Beyond observing structural features with seismic imaging, a key to understanding these

processes lies in understanding the deformation history. Dislocation-creep accommodated strain of mantle minerals such as olivine leads to the development of elastically anisotropic fabric, which causes birefringence of shear waves. Shear wave splitting methods, the most common of which is the Silver and Chan method [Silver and Chan, 1991], that measure this effect have been used for over four decades to investigate deformational fabrics at depth. They are fundamentally based on the following process: when a shear wave propagates through an anisotropic medium, it is split into two perpendicular components with one component travelling faster than the other.

Common shear wave splitting methods use core refracted shear waves such as SKS to extract the apparent splitting parameters of  $\phi$  and  $\delta t$ , which correspond to the polarization of the fast component, also referred to as the fast velocity axis (FVA), and the delay time between the two components, respectively. These azimuth measurements can then be used to infer the geometry and degree of anisotropy of a single anisotropic layer with a horizontal symmetry axis [e.g. Silver and Chan [1991]].

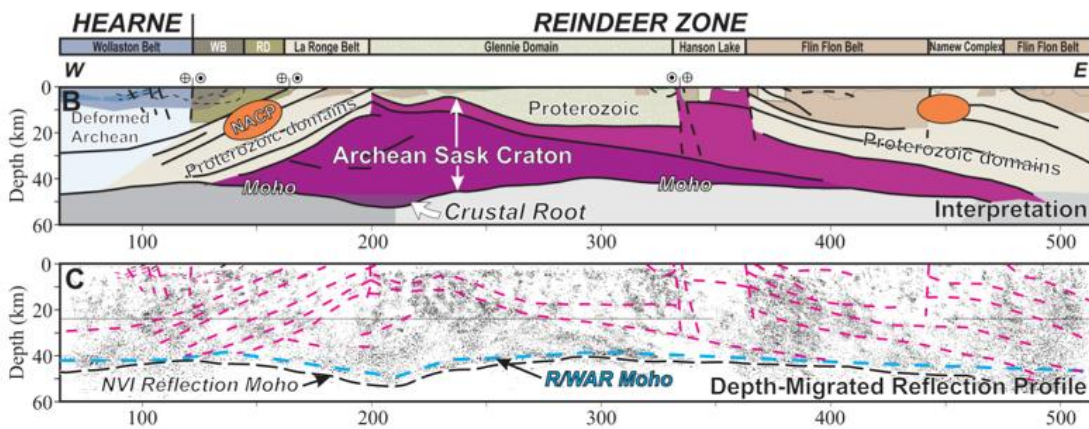


**Figure 6.** Cross section through Sask craton from Lithoprobe [Hammer et al., 2011]. (Top) Simplified interpretation based on geological, seismic reflection/wide-angle reflection, and magnetotelluric studies showing the geometry of the trapped Archean Sask craton. (Bottom) Depth-migrated seismic section with pink lines showing dominant structures. The reflection and refraction inferred Mohos are shown by the black and blue dashed lines, respectively.

Ongoing flow of the asthenosphere induced by lithospheric motion is probably the most likely cause of upper mantle anisotropy [e.g. *Long and Silver, 2009*]. Additionally, anisotropic fabrics from past deformational events can be ‘frozen’ within the mantle lithosphere, and are likely to be present in cratonic regions, where the lithosphere is old, cold, and thick. In such regions, valuable information recorded by these ‘frozen-in’ fabrics can help us better understand the processes that formed the continents billions of years ago.

In this study we investigate anisotropy beneath two long-standing broadband seismic stations along the continent-forming Trans Hudson Orogen (**figure 5**). Station FFC is located near Flin Flon, Manitoba, Canada, on the eastern edge of the Proterozoic Sask craton. Two collisional episodes at FFC, beginning with the continent-continent collision of the Archean Sask and Hearne cratons around 1.84 Ga., and followed by the collision of that amalgamated entity with the Superior craton around 1.82 Ga., are responsible for the final assembly of the North American craton in this region [*Hoffman, 1989; Andsell, 2005; Hammer et al., 2011*]. RSSD is located in the Black Hills of South Dakota, on the eastern margin of the Wyoming craton. The Trans Hudson Orogen extends into the Northern United States where it is recognized from outcrops in the Black Hills. In this region, the Trans Hudson Orogen resulted from the collision between the Wyoming and Superior cratons [*Whitmeyer and Karlstrom, 2007*].

### ***2.2.3 A multiple layer approach***

In the presence of two anisotropic layers, a shear wave will be split twice; however, the ~10s dominant period of the observed SKS waves is much larger than the ~1s time difference between split shear waves. Hence, a multiply split SKS wave has no distinctive features that would distinguish it from a wave split only one time. The apparent splitting parameters measured under the assumption of a single layer when two layers are in fact present cannot be directly related to

any individual layer, but they will display systematic variations that are dependent on the geometry of the incoming ray-path. When observed, these variations are often used to diagnose the presence of two layers. Shear wave splitting studies from a variety of continental regions have identified these patterns and hypothesized the presence of multiple anisotropic layers [*Silver and Savage, 1994; Ozalaybey and Savage, 1995; Silver and Long, 2011*].

Geologically, the existence of multiple layers of anisotropy beneath the continents is not difficult to postulate. For a lithosphere that is relatively new, hot, and thin, the alignment of minerals may be consistent with the asthenospheric strain field induced by plate motion, and the single layer approximation is most likely appropriate. But in regions where the lithosphere is old, cold, and thick, plate-motion driven anisotropy may be actively forming in the asthenosphere, and 'frozen-in' fabrics from past deformation may also be present in the lithosphere. In such regions, valuable information recorded by these fabrics may be lost in the single layer approximation.

The cross convolution method [*Menke and Levin, 2003*] provides an alternative to common shear wave splitting methods by using the radial and tangential impulse response to examine anisotropy. With this approach, anisotropic layering and other features of near-arbitrary complexity can be modeled, as long as the radial and transverse impulse responses are independent of each other. Notably, this method allows for full quantification of probability density functions of individual parameters, allowing us to describe and compare the relative likelihood of each parameter to take on values found for multiple anisotropic layer models.

*Yuan et al., [2007]* used an approach based on cross convolution in conjunction with a directed Monte Carlo search algorithm, the Neighborhood Algorithm [*Sambridge, 1999a, 1999b*], to estimate the effects of complex anisotropy on SKS data from a dense broadband array in Billings, Montana. That study found that a model with two dipping layers of anisotropy was better able to explain the data than the common one flat layer model.

In this study we build upon the method put forth by *Yuan et al* [2007] to investigate anisotropy beneath FFC and RSSD. SKS data from the two stations is tested and ranked for four of the simplest upper mantle anisotropic parameterizations. For each parameterization, a lowest misfit solution is found via the Neighborhood Algorithm by optimizing the fit of cross-convolved data with synthetic data. Quantitative assessment of model ensembles generated by the Neighborhood Algorithm is performed via inspection of model Posterior Probability Density functions, which are used to extract parameter expectations and standard deviations. Visual inspection of the Posterior Probability Density 1- and 2-D marginals is used to assess parameter covariance. We then employ an F-test to rank best fitting model solutions for the different parameterizations with the goal of determining whether we can reject certain parameterizations on the basis of their inability to significantly account for the data. We also perform a series of synthetic tests in an attempt to determine the limits of our given data sets in resolving complex structure.

## **2.3. Data and Methods**

### ***2.3.1 Shear Wave Data Selection***

Teleseismic shear wave data in this study comes from two long-standing broadband seismic stations: FFC and RSSD. Both stations are components of the Global Seismic Network and have over 10 years of data archived. Station FFC is located near Flin Flon, Manitoba, Canada, within Precambrian granitic gneiss. FFC contains a Streckeisen Model STS-1/VBB 3 component system for broadband and long period channels recorded at 20 sps and 1 sps, respectively, and has a flat response to ground velocity from 0.1 to 360 sec [*Streckeisen, 1987*]. RSSD is located in the Black Hills of South Dakota, within Mississippian age limestone, contains a Geotech KS-54000 Borehole Seismometer that has a flat velocity response from 0.003 to 5 Hz [*Ringler and Hutt, 2010*]. Neither station required a correction for instrument response.

**Table 1. Event Table for FFC and RSSD**

Station	Event Date	Back Azimuth	Signal/Noise	D.O.F.
FFC	1993_272_22	1.608	2.321	35
FFC	1994_068_23	248.78	19.126	38
FFC	1994_090_22	247.299	8.771	22
FFC	1995_017_16	247.756	7.12	32
FFC	1995_136_03	4.121	10.535	29
FFC	1997_145_23	241.649	13.535	21
FFC	1999_177_22	248.584	6.227	20
FFC	2000_127_13	265.924	4.951	14
FFC	2002_181_21	248.033	16.687	27
FFC	2002_231_11	247.153	14.613	14
FFC	2003_133_21	259.917	4.739	34
FFC	2003_146_23	313.443	3.009	22
FFC	2003_163_08	277.193	9.882	21
FFC	2011_210_07	246.846	9.195	29
RSSD	2000_166_02	243.711	14.017	27
RSSD	2000_199_22	4.191	9.094	25
RSSD	2001_346_12	256.291	4.436	21
RSSD	2002_062_12	4.342	4.384	20
RSSD	2002_148_16	318.467	4.932	25
RSSD	2004_096_21	4.027	3.595	50
RSSD	2005_288_15	317.701	5.769	13
RSSD	2006_209_07	317.417	8.528	28
RSSD	2006_219_22	257.435	5.436	47
RSSD	2008_167_01	247.579	3.503	36
RSSD	2008_185_03	243.653	4.17	23
RSSD	2009_194_18	317.897	8.363	18
RSSD	2009_230_21	240.891	7.497	22
RSSD	2011_018_20	10.967	7.946	23

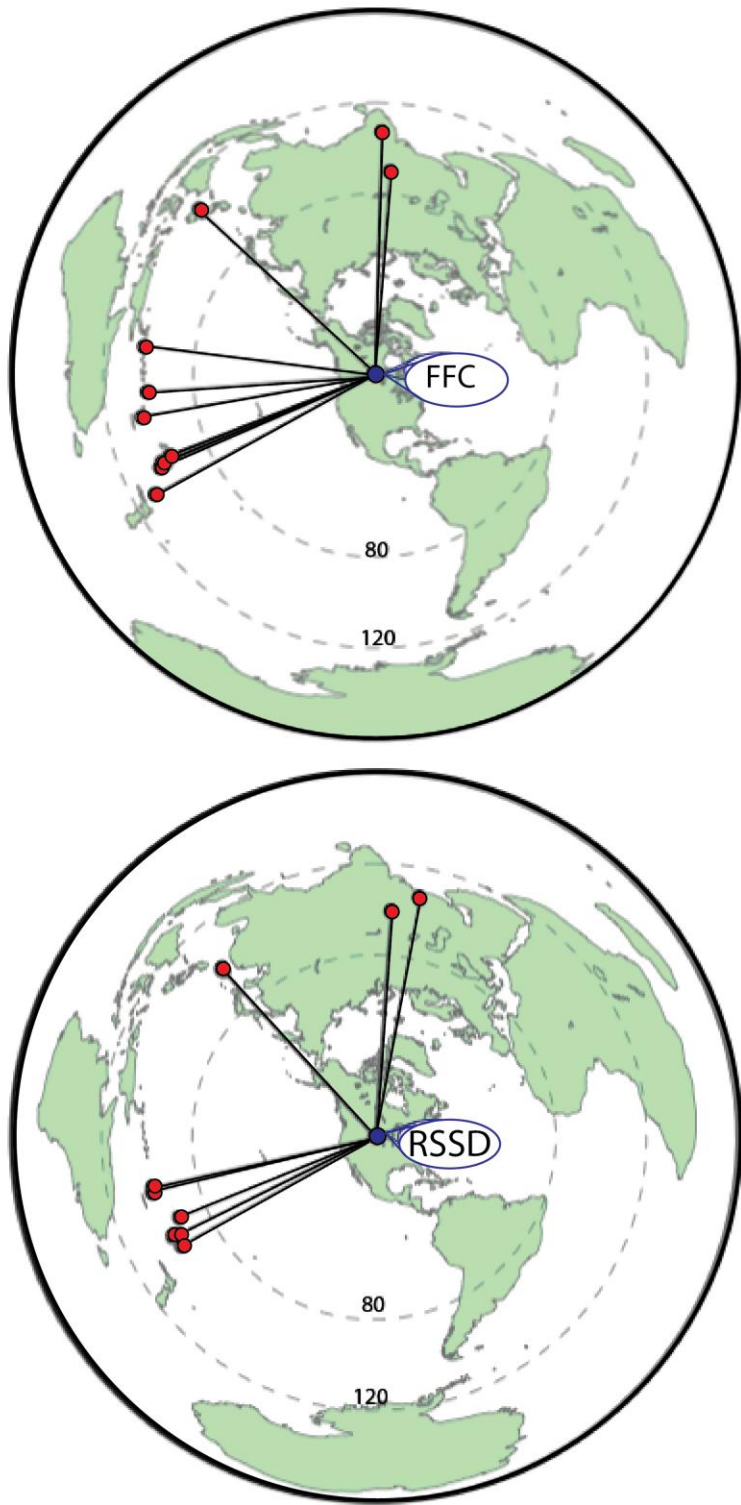


**Figure 7.** Event location maps for FFC (top) and RSSD (bottom). The dashed circles give distances of 80° and 120°, for reference.

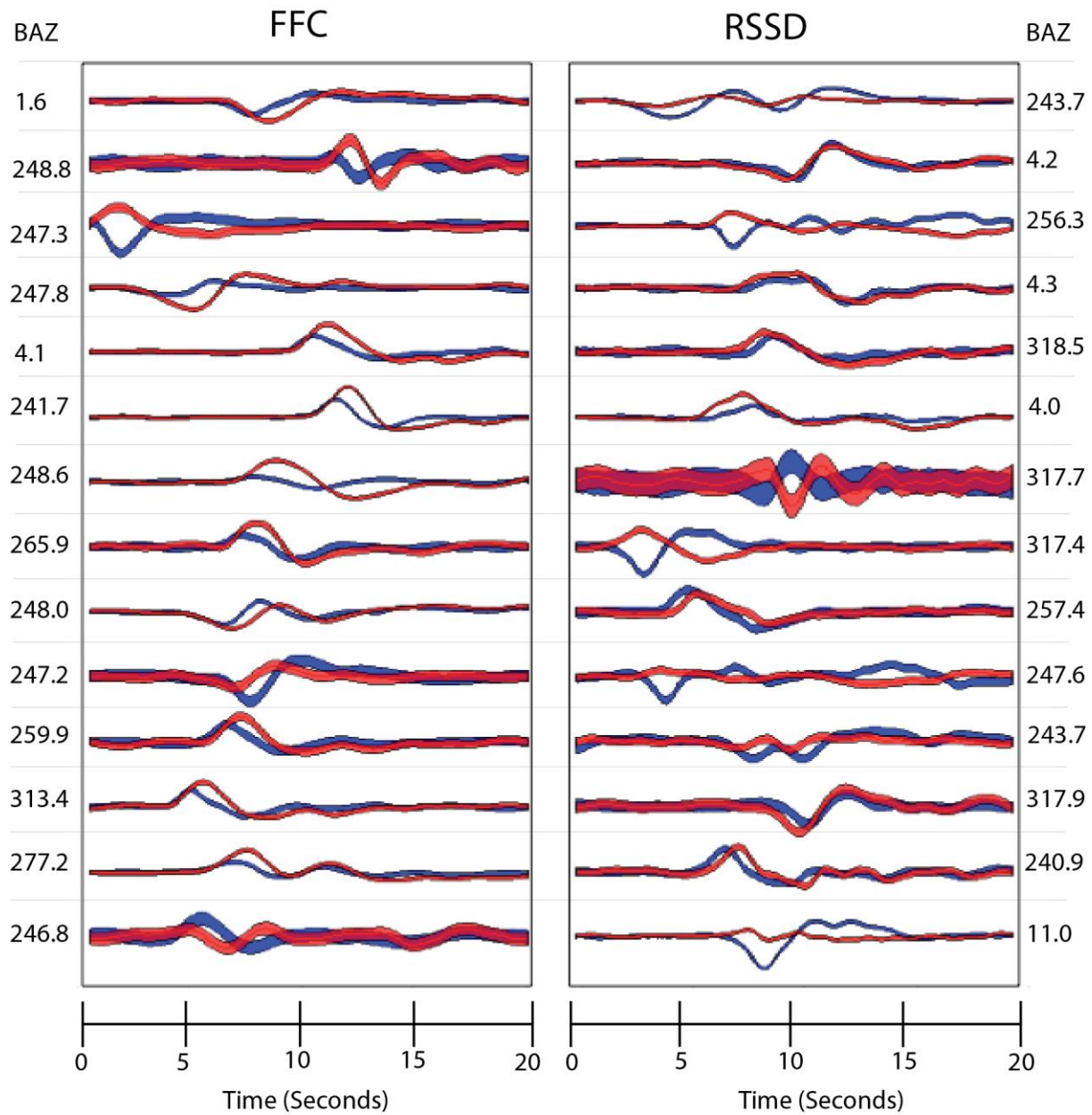


**Figure 8.** SKS waveforms for FFC and RSSD. The radial and transverse components are plotted in red and blue, respectively, with line thicknesses directly proportional to the standard error estimated for each waveform pair.

Events with a high signal to noise ratio ( $>3$ ) and no other phase arrivals within 10 seconds of the SKS window are subjected to a visual inspection, and those satisfying all three criteria are deemed high quality. 14 events (**Table 1**) were selected for both the FFC and RSSD data sets, providing a back azimuthal distribution of  $\sim 100^\circ$  at both stations (**figure 7**). A common window

length of 20 seconds is used for each event waveform pair, with the onset of the window automatically set at 5 seconds prior to the onset of the radial SKS signal. The error associated with waveform is taken from the signal to noise ratio, calculated by taking the root mean-square amplitude of the noise, defined by the 10 second long window prior to the onset of the SKS window, and dividing it by that of the signal (**figure 8**). The degrees of freedom for each event waveform pair are calculated from the spectral bandwidth of the data [*Jenkins and Watts, 1968; Silver and Chan, 1991*]. Events are normalized by the sum of squared amplitudes of the radial and transverse components in order to remove amplitude effects.

### ***2.3.2 Silver and Chan Method Analysis***

We conduct a preliminary analysis using the Silver and Chan method, in order to test for variations in apparent splitting parameters as described in **section 2.2.3** [*Silver and Chan, 1991*].

### ***2.3.3 Model Parameterizations***

In this study, we test the fit of our SKS data to four of the simplest upper mantle anisotropic velocity model parameterizations given by the following anisotropic Earth models. To simulate upper mantle conditions, in which lattice preferred orientation of olivine is the primary contributor to azimuthal anisotropic fabric development, we assume a hexagonal anisotropy system with a fast velocity axis, and two orthogonal slow velocity axes. Hexagonal anisotropy should account for about 80% of the effects of fully orthorhombic anisotropy [*Becker et al., 2003*]. Our models consist of an upper 40 km thick isotropic half space simulating an isotropic crust, either one or two, flat or dipping, 100 km thick anisotropic layers below, and a lower 100 km thick isotropic half space (see **figure 9**). Layer thicknesses, densities, and layer velocities are all fixed according to *Yuan et al., [2007]* to target upper mantle anisotropy. The contribution of crustal anisotropy is minimal [*Iidaka and Niu, 2001*], and the ray paths of the SKS diverge so far from each other at the D" depth

that the effects of D'' anisotropy can essentially be considered noise. Our four different model parameterizations tested contain either two or three parameters per layer and are defined as follows: Models A and B consists of one anisotropic layer with flat and dipping fast velocity axes (FVA) respectively, and models C and D consist of two anisotropic layers with flat and dipping respective FVAs. FVA strike is measured as positive clockwise from the North, and dip is measured as positive downwards with respect to the horizontal along the FVA strike direction.

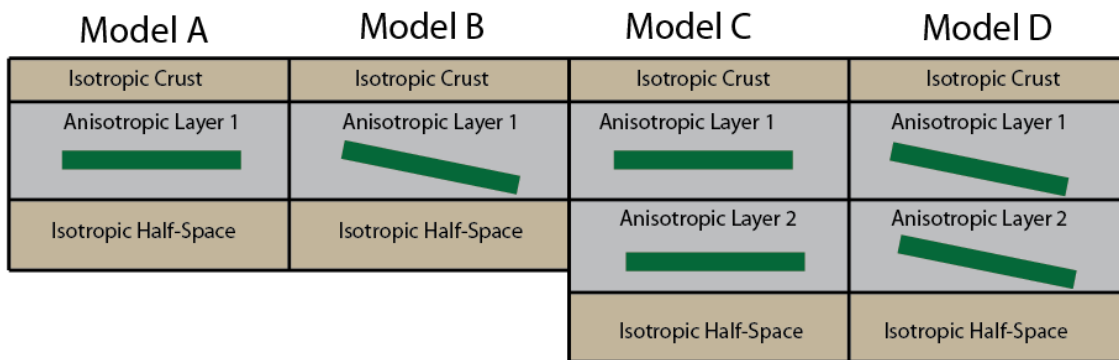


**Figure 9.** Cartoon of four model parameterizations tested. Models A and B are single layer anisotropy models with model A having a flat FVA and model B having a potentially dipping FVA. Model C is a two layer model with both layers having a flat FVA, and model D is a two layer model with both layers having a potentially dipping FVA. For all models, the crustal thickness is fixed at 40 km, and each anisotropic layer thickness is fixed at 100 km.

### 2.3.4 Searching Parameter Space

Menke and Levin [2003] showed that, for a split shear wave propagating through an arbitrary amount of anisotropic layers, the observed radial trace convolved with the tangential impulse response of the anisotropic layers will be equal to the observed tangential convolved with the radial impulse response:

$$(1) \quad r * T(\mathbf{m}) = t * R(\mathbf{m}),$$

where  $r$  and  $t$  are the observed radial and tangential traces,  $\mathbf{m}$  is the vector of model parameters that describes the anisotropy in all the layers, and  $R$  and  $T$  are the radial and tangential impulse

response of the anisotropic layers for the given event parameters. Hence, one can search over all reasonable  $\mathbf{m}$  to find the parameters that minimize the misfit, defined as

$$(2) \quad ((r * T(m) - t * R(m))^2.$$

Because a full grid search becomes computationally cumbersome for higher model parameterizations, we instead employ a type of direct Monte Carlo search algorithm, the Neighborhood Algorithm [Sambridge, 1999a, 1999b], to map the misfit surface associated with each of our anisotropic model parameterizations. The Neighborhood Algorithm approach uses an iterative functionality in which the parameter space is partitioned into Voronoi (nearest-neighbor) cells through which a random walk-through is used to map the misfit surface. The information carried in that map is then used to re-partition the parameter space so that the search is concentrated in regions where the misfit is minimized [Sambridge and Mousegarrd, 2002].

### 2.3.5 Model Inference

To assess the optimal model parameterization, and to calculate confidence bounds, the misfit is divided by an estimation of the error and the degrees of freedom to calculate a reduced chi-squared statistic following the formula set out in Yuan *et al.* [2007]

$$\chi_v^2(\vec{m}) = \frac{1}{v} \sum_{i=1}^N \frac{\sum_{j=1}^k (R^i * t^i(\vec{m}) - T^i * r^i(\vec{m}))^2}{\sum_{j=1}^k \left[ (R_{RMS}^i * r^i(\vec{m}))^2 + (2(R_{RMS}^i * r^i(\vec{m}))(T_{RMS}^i * t^i(\vec{m}))) + (T_{RMS}^i * t^i(\vec{m}))^2 \right]}.$$

Here,  $i$  indexes the  $N$  events,  $v$  is the number of degrees of freedom,  $R^i$  is the observed radial trace for the  $i$ th event,  $t^i(\mathbf{m})$  is the synthetic tangential impulse response,  $T^i$  is the observed transverse trace, and  $r^i(\mathbf{m})$  is the synthetic radial impulse response. The numerator and denominator are both summed over the number of points in each event time series,  $k$ . To normalize the misfit by estimated error, the root-mean-square value of the observed radial and tangential pre-SKS arrival

noise is calculated. This value is converted to a  $k$  point time series representing the estimated error in the radial and tangential traces ( $R_{RMS}^i$ , and  $T_{RMS}^i$ ). Using the root-mean-square level of the pre-SKS noise is a small change from the *Yuan et al.* [2007] paper which was able to assess the standard error of the mean for seismograms observed at a number of nearby stations in a seismic array. This is impossible in the current analysis since we are only considering a single station at a time.

The reduced chi-squared estimates are converted to probability density functions (PDF) assuming a multivariate Gaussian probability function

$$P(\mathbf{m}) = k \exp \left( -\frac{\nu}{2} \chi^2_{\nu}(\mathbf{m}) \right)$$

where  $k$  is a constant that normalizes the total probability to unity,  $\nu$  is the number of degrees of freedom, and  $\chi^2_{\nu}$  is the reduced chi-square value [*Yuan et al.*, 2007].

The PDFs are then used to calculate quantities such as the model expectation (mean) and the 1- and 2-D posterior marginal probability density functions: In order to better visualize the probability density functions associated with *individual* parameters (i.e. 1-D), or a pair of parameters (i.e. 2-D), we integrate over all values of the other variables.

### **2.3.6 Synthetic Testing**

Synthetic tests using the same event parameters (back-azimuth, incidence angle, and polarization) as the true data set are conducted to investigate the ability of our data set coverage to constrain the anisotropic models found by our search. The synthetic waveforms are generated using the anisotropic impulse response calculated via the ray theoretical method of *Fredricksen and Bostock* [2000]. To assess the ability of our given event distribution (rather than data quality) to resolve complex structure, we refrain from adding noise to our synthetic waveforms.

Because our synthetic waveforms have no noise added, we cannot calculate normalize the misfit by the errors (which are 0) to calculate meaningful chi-squared values, and therefore cannot

generate valid PDFs. Instead, we perform bootstrap analyses on our synthetic data, in which random events are selected with replacement and subjected to the search method described above in an iterative manner [Efron and Tibshirani, 1993]. Due to their distribution independence, bootstrap results can be used to assess how accurately our data follows our assumption of a chi-square distribution [Sambridge, 1999b]. Additionally, bootstrapping allows us to examine biases that result from limited sampling of the data set.

## 2.4. Results

### 2.4.1 *Silver and Chan Method Results*

Results from a *Silver and Chan* [1991] method analysis of our data are shown in **figure 10**. At FFC, delay times range from  $\sim 0.5$  to 1 seconds for all events except two, which have delay times greater than 1.5 seconds. Results for FVA are similarly distributed, with the majority of events ranging from  $25$ - $50^\circ$ , and two outliers that are between  $100$  and  $150^\circ$ . For both delay time and FVA, the two outlier events have the widest confidence bounds, while the tightly constrained results show better agreement. At RSSD, events from a back azimuth window of  $0$ - $15^\circ$  produce small delay times (less than 0.6 seconds, while events from a back azimuth window of  $240$ - $330^\circ$  produce a variety of delay times that range up to 2.5 seconds. Events from the  $240$ - $330^\circ$  back azimuth window have well-constrained FVAs that cluster around  $25^\circ$ , but events from the  $0$ - $15^\circ$  back azimuth window find well-constrained FVAs that cluster around  $125^\circ$  and  $50^\circ$ . Neither FFC nor RSSD apparent splitting parameters exhibit a clear pattern with respect to back azimuth.

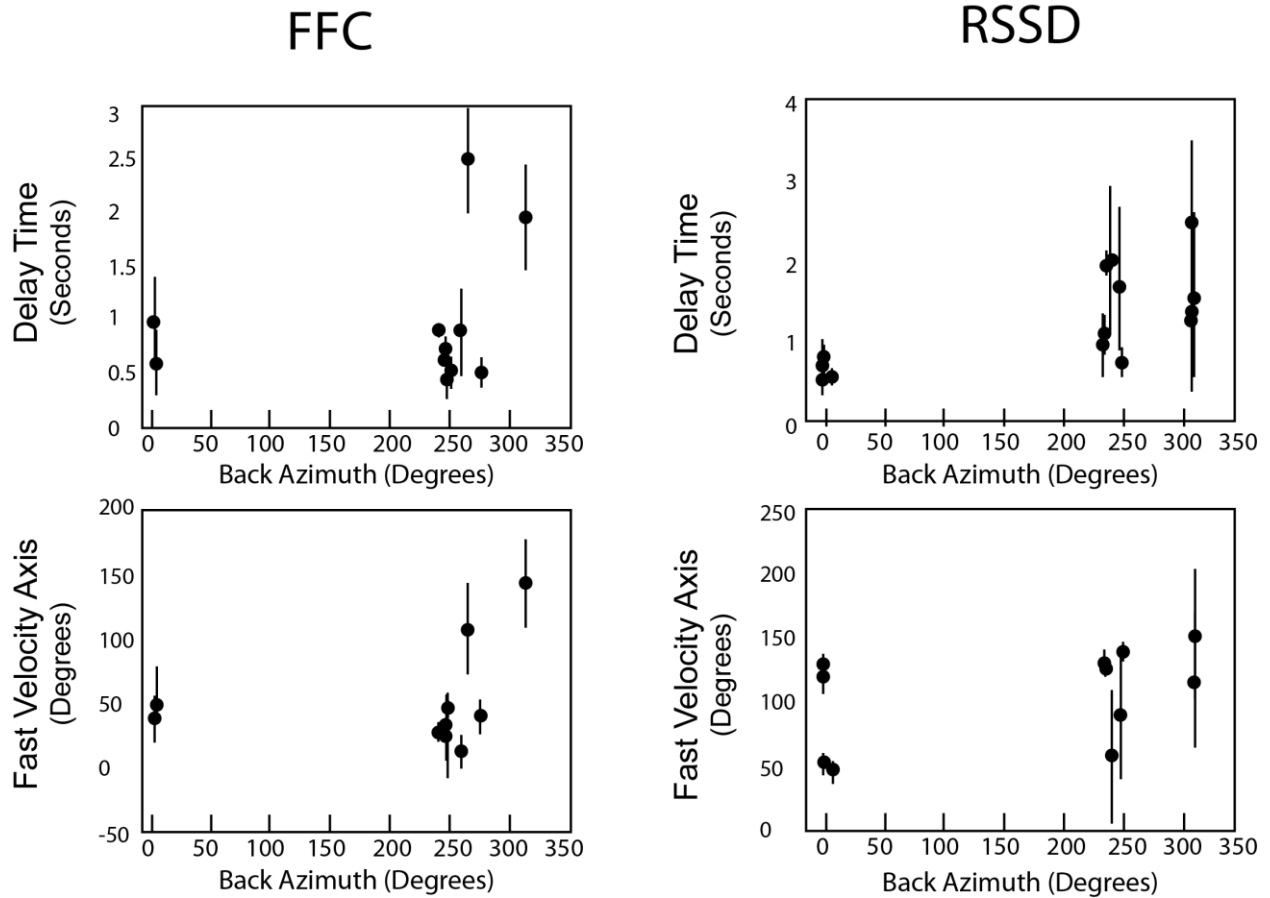


**Figure 10.** *Silver and Chan* [1991] method results for FFC and RSSD. Error bars show 95% confidence limits.

## 2.4.2 FFC

### 2.4.2.1 Weighting events by back azimuth

To assess whether an uneven distribution of events at FFC, where all but 3 of our 14 events fall within a back azimuth window of 245-280°, leads to bias in the solution, we analyze FFC both with and without weighting events by back-azimuth. For the weighted data set, events were classified as either inside or outside of the back azimuth window that ranged from 245-280°. Events outside of that bin were replicated until the number of events outside equaled the number of events inside the bin. Best fitting parameter solutions, and associated 95% confidence bounds

(shown in brackets), for each model are shown in **tables 2 and 3** for the un-weighted and weighted data sets respectively.

In both the weighted and un-weighted cases, our two simplest models, A and B (having two and three free model parameters respectively; figure 9), find a similar upper layer solution with comparable 95% confidence limits of  $\sim 2.9\%$  anisotropy at a FVA strike of  $\sim 40^\circ$ . Both data sets find the same upper layer solution in the simplest two-layer model, C, and agree on a strike of  $\sim 70^\circ$  in the lower layer; however, the 95% confidence bounds are significantly wider for the un-weighted data. The two data sets show the most disagreement in the highest parameterization, model D. For the un-weighted data, the model D upper layer solutions for both % anisotropy and strike FVA is well-constrained, but falls entirely outside of the 95% confidence bounds of the upper layer results from all three models with fewer free parameters. Furthermore, model D places a  $\sim 90^\circ$  dip in the upper layer. As  $90^\circ$  is the upper bound allowed for dip; this result raises skepticism since it essentially is the same as putting zero anisotropy in the lower layer. Conversely, the model D result for the weighted data has tight confidence bounds for all parameters and agrees with the upper layer results for the lower parameterizations (**figure 11**).

**Table 2: Model results for un-weighted FFC data set.**

<b>Model</b>	<b>A</b>	<b>B</b>	<b>C</b>	<b>D</b>
<b>% Anisotropy Layer 1</b>	39.02 [38.57, 40.38]	2.86 [2.76, 2.96]	2.81 [1.96, 3.17]	0.60 [0.55, 0.75]
<b>Strike Layer 1</b>	2.93 [2.88, 3.01]	38.44 [37.54, 42.06]	34.82 [32.11, 39.35]	13.12 [12.21, 17.64]
<b>Dip Layer 1</b>		18.09 [10.40, 18.54]		88.19 [88.19, 89.55]
<b>% Anisotropy Layer 2</b>			0.60 [0.30, 2.06]	2.46 [2.36, 2.56]
<b>Strike Layer 2</b>			69.65 [38.89, 75.98]	47.94 [46.13, 49.75]
<b>Dip Layer 2</b>				14.92 [13.57, 16.28]
<b>Degrees of Freedom</b>	355	354	353	351
<b>Chi-Squared Reduced</b>	1.87	1.86	1.82	1.79

**Table 3: Model results for weighted FFC data set.**

<b>Model</b>	<b>A</b>	<b>B</b>	<b>C</b>	<b>D</b>
<b>% Anisotropy Layer 1</b>	3.03 [3.1, 3.13]	3.07 [2.86, 3.12]	2.86 [2.51, 3.12]	3.27 [2.96, 3.52]
<b>Strike Layer 1</b>	42.63 [40.83, 43.08]	42.06 [40.25, 43.87]	38.44 [23.97, 42.96]	34.82 [29.40, 39.35]
<b>Dip Layer 1</b>		11.31 [6.78, 14.92]		16.73 [11.31, 20.80]
<b>% Anisotropy Layer 2</b>			1.21 [0.80, 1.56]	0.40 [0.10, 0.85]
<b>Strike Layer 2</b>			74.17 [70.55, 78.69]	47.94 [46.13, 49.75]
<b>Dip Layer 2</b>				27.59 [24.87, 37.09]
<b>Degrees of Freedom</b>	355	354	353	351
<b>Chi-Squared Reduced</b>	1.75	1.75	1.67	1.6

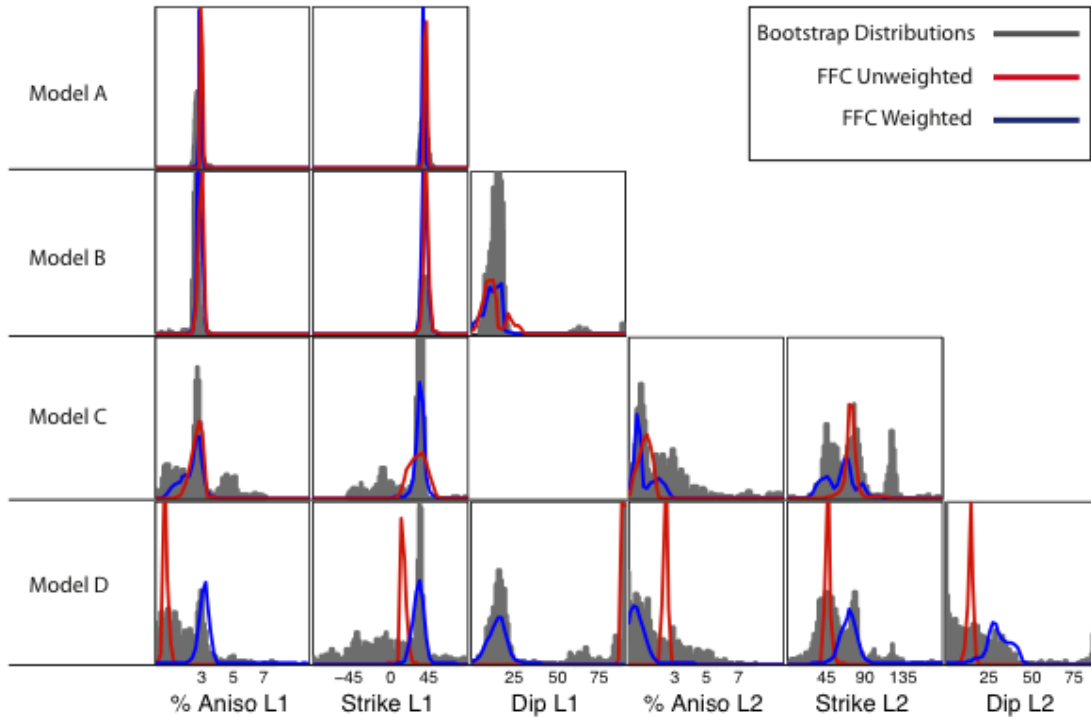


**Figure 11.** Comparison of histograms of bootstrap results for FFC (grey) with un-weighted (blue) and weighted (red) PDF marginals for FFC. For each individual plot, the vertical axis is fixed to 150 for the number of bootstrap iterations, and 0.75 for PDF marginal probability. For models A and B, there appears to be little difference between the fit of the un-weighted and weighted data. For model C and D, PDF marginals for the weighted data provide a better fit the bootstrap distributions both in shape and peak location.

A 1000 iteration bootstrap analysis of the un-weighted data set was conducted, and individual parameter histograms are shown in **figure 11** with corresponding 1-D PDF marginals for both the un-weighted and weighted data sets superimposed. The bootstrap distributions correlate well with the un-weighted PDF marginals in all cases except for model D, where distributions differ in shape and peak location for each of the six parameters. Alternatively, the weighted PDF marginals for model D more accurately capture the corresponding bootstrap distributions. As one would expect [*Silver and Savage, 1994*], these results demonstrate that the lower-parameterized models are less dependent on back azimuthal distribution, while the higher parameterizations become increasingly biased. We use these observations as justification for weighting our data set

according to back azimuth distribution, and all subsequent inference is made with respect to the weighted data.

#### 2.4.2.2 Model Inference and Ranking

1- and 2-D PDF marginals are produced to allow for visual inspection of the multidimensional model ensembles and are shown in **figures 12** and **13** respectively. The 1-D marginals show strong agreement on parameter solutions across all four models. Model B results indicate that there is little to no effect on strike or % anisotropy when allowing for one layer to dip. *Chevrot et al.* [2003] quantified the effects of a dipping axis of symmetry on SWS measurements and found that a significant dip (greater than  $20^\circ$ ) results in systematic variations of splitting parameters with back-azimuth, while dips less than  $20^\circ$  have little to no effect on splitting parameters. The FFC results appear to support their findings. Our higher parameterizations (models C and D) indicate that the upper layer solution is quite stable when allowing for a second layer of anisotropy, which is not surprising considering that both models don't allow for more than minimal (1.5%) anisotropy in the lower layer. The solution for lower layer dip in model D is greater than  $20^\circ$  and unlike the dip solution in model B, does appear to correlate with a reduction in % anisotropy and change in FVA orientation of that layer when compared to model C results.

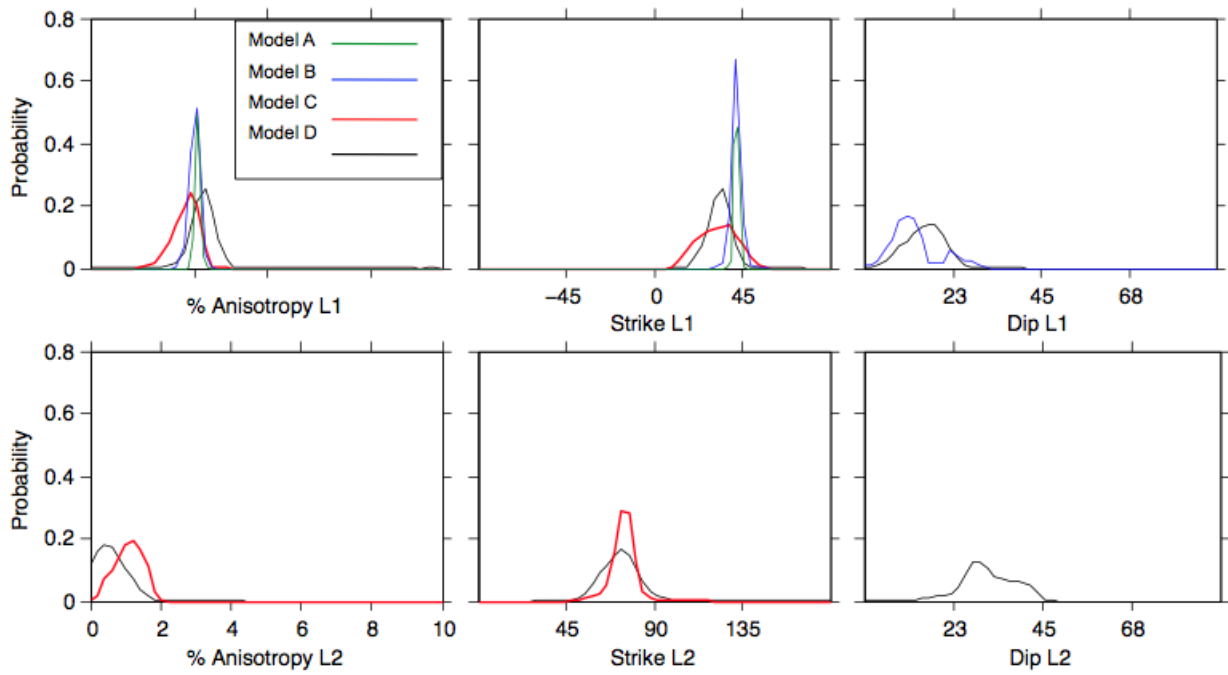


**Figure 12.** 1-D PDF marginals for weighted FFC data set. Each subplot contains individual parameter solutions for each relevant model parameterization (shown by color according to legend in the upper-left plot). 'L1' and 'L2' refer to the upper and lower layers, respectively. The 1-D PDF marginals are found by integrating over the other model parameters and hence properly account for correlated model errors.

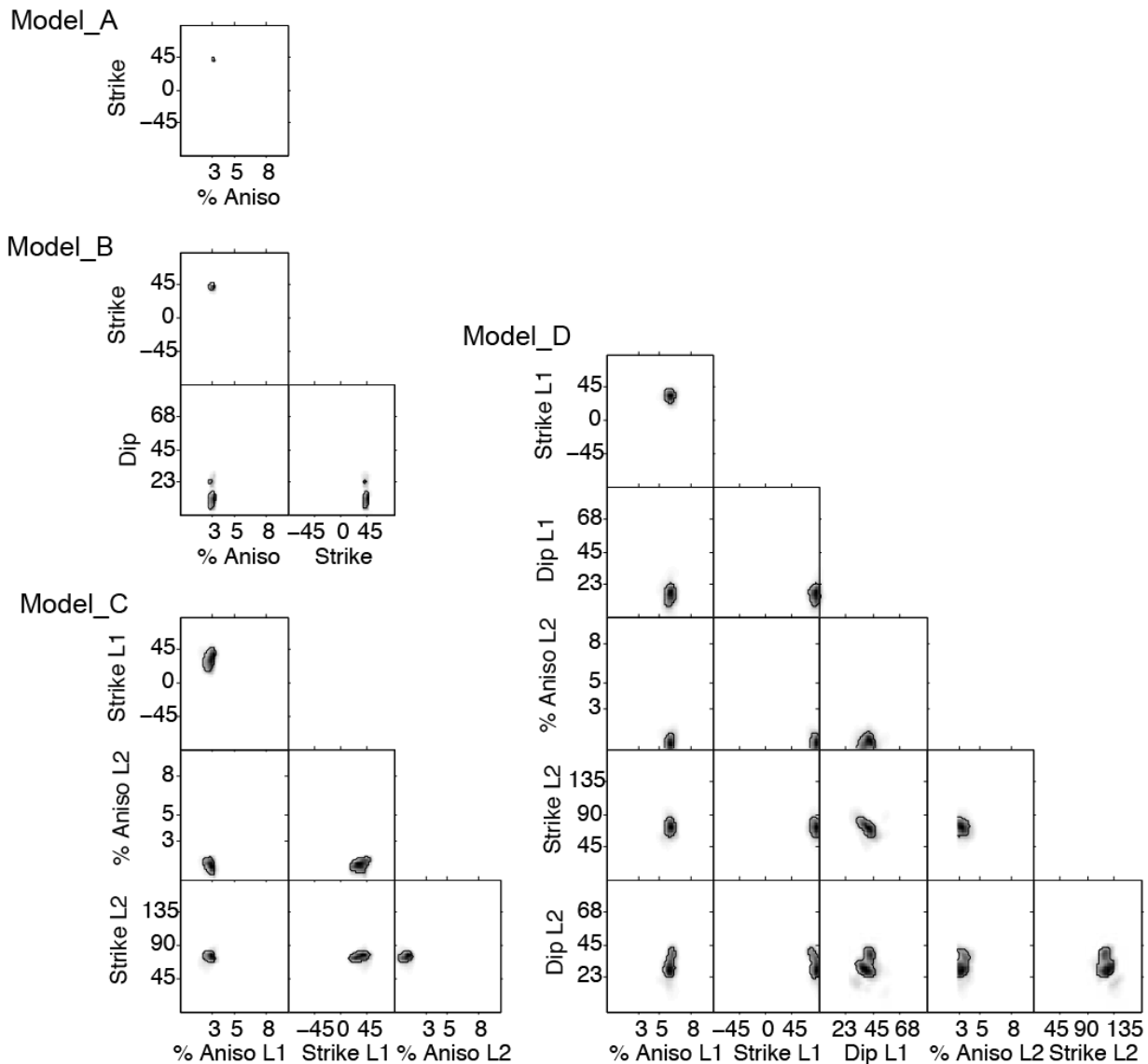


**Figure 13.** 2-D PDF marginals for weighted FFC data set. Each subplot is labeled by the model parameterization. The darker shading corresponds to higher probabilities and a contour line outlines the 80% probability contour. The model parameter names and values are labeled along the bottom and left sides of the matrices. Strike is rendered in degrees positive clockwise with respect to North, and dip in degrees positive downward from horizontal.

Inspection of the 2-D marginals (**figure 13**) shows that solutions are generally compact and uni-modal in models A, C, and D, indicating good resolution of the model parameters with little parameter correlation. The 2-D marginals also show that the area of acceptable solutions becomes wider with increasing parameterization, which is to be expected due to increasing non-linearity and

non-uniqueness associated with more complex models. Model B shows a bi-modal solution for dip that does not appear to be correlated with % anisotropy or strike.

Given that model D has more free parameters than the other models, it is expected it will fit the data better than the other models. However, it is also instructive to be parsimonious in the model complexity allowed, and consider whether all the free model parameters are necessary to fit the data. In order to determine which of our models optimally explains the data, we consider three null hypotheses: 1) model A fits the data as well as model D; 2) model B fits the data as well as model D; and 3) model C fits the data as well as model D. To evaluate these null hypotheses, we examine the various models' goodness of fit with the reduced chi-squared statistic, and compare the significance of that fit between models using the F-test (**table 3; figure 14**).

The F-test, as performed here, tests the confidence with which the null hypothesis can be rejected. Essentially it is a statistical measure of whether the reduced chi-squared value of Model D is significantly better than the model in question. F-test results show that null hypotheses 1, 2, and 3--that models A, B, and C are sufficient to fit the data-- can be rejected with 78%, 80%, and 62% confidence against model D, respectively. At the 2-sigma confidence level (95.4%), we fail to reject any of the null hypotheses. At 1-sigma confidence (68.3%), the null hypothesis for models A and B, can be falsified, but not model C.

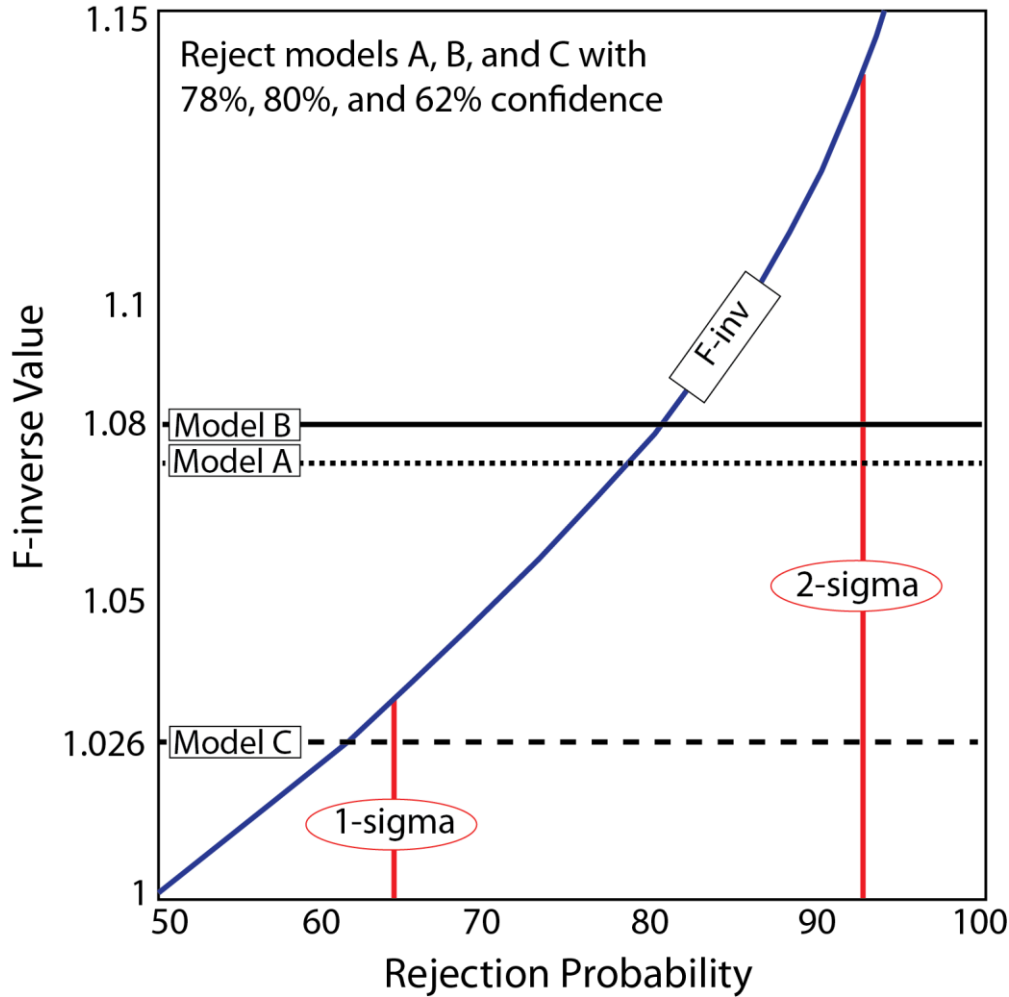


**Figure 14.** F-test results showing the reduced model rejection probabilities with respect to the full model (D). The solid blue line plotted is the F-inverse curve using the average number of degrees of freedom of the four parameterizations. 1- and 2-sigma confidence limits are shown by red lines.

#### 2.4.2.3 Synthetic Testing

To test whether the back azimuthal distribution of the data is sufficient to constrain the various models, two synthetic waveform data sets (FFC\_SD\_A and FFC\_SD\_D) are created using the anisotropic parameters from the best fitting solution for models A and D respectively. We choose to test these two models because model A is the most commonly used parameterization, and model D is our highest parameterization. To evaluate our synthetic tests, we define the *properly parameterized* model as the one in which the dimensionality of the model used to generate the

synthetic data set is equal to the dimensionality of the model tested. *Under-* and *over-parameterized* models are defined respectively as those whose dimensionalities are lower and higher than that of the model used to generate the synthetic data. We conduct bootstrap analyses on FFC\_SD\_A and FFC\_SD\_D.

1- and 2-D bootstrap results from testing of FFC\_SD\_A are shown in **figures 15** and **16**, respectively. The 1-D distributions show that each of our four model parameterizations is able to resolve the input anisotropic parameterization, and for the *properly parameterized* model (A), the solution is close to unique. For model B, we see that allowing one layer to dip when the true model is flat does not affect the solutions for % anisotropy and strike. We also see in model B that possible dips allowed by the data are limited to less than  $20^\circ$ , suggesting the fast-axes are near-horizontal [Silver and Savage, 1994; Chevrot and Van Der Hilst; 2003]. The 1-D distributions for models C and D show that *over-parameterized* models (B, C, D) properly resolve the upper layer input parameters (**figure 15**).

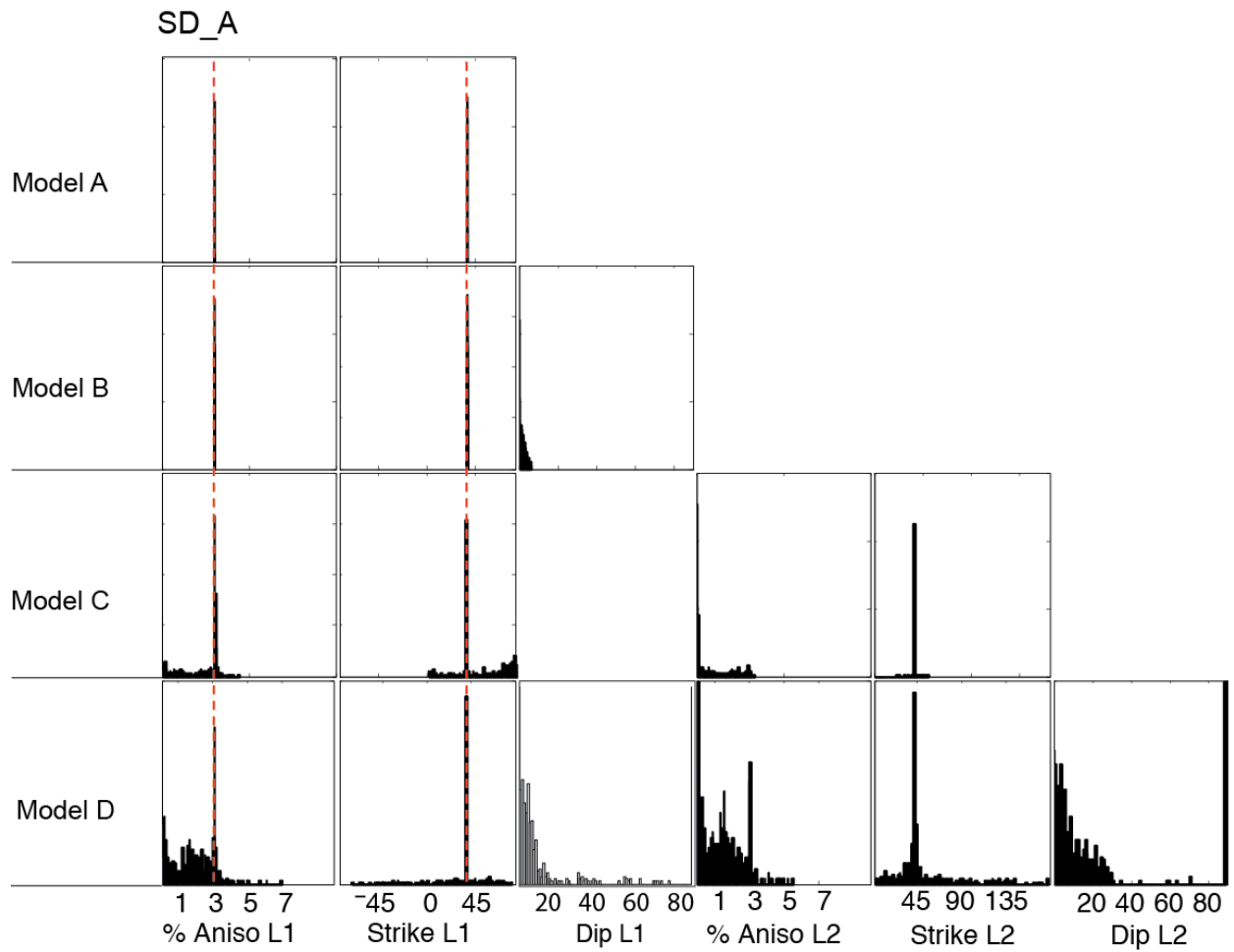


**Figure 15.** 1-D bootstrap distributions for FFC\_SD\_A. Each subplot contains an individual parameter bootstrap distribution. Columns correspond to the parameter displayed and are labeled on the bottom of the matrix. Rows correspond to the model for which the parameter is found and labeled on the left of the matrix. Strike is rendered in degrees positive clockwise with respect to North, and dip in degrees positive downward from horizontal. The red dashed lines represent parameter values used to generate FFC\_SD-A.

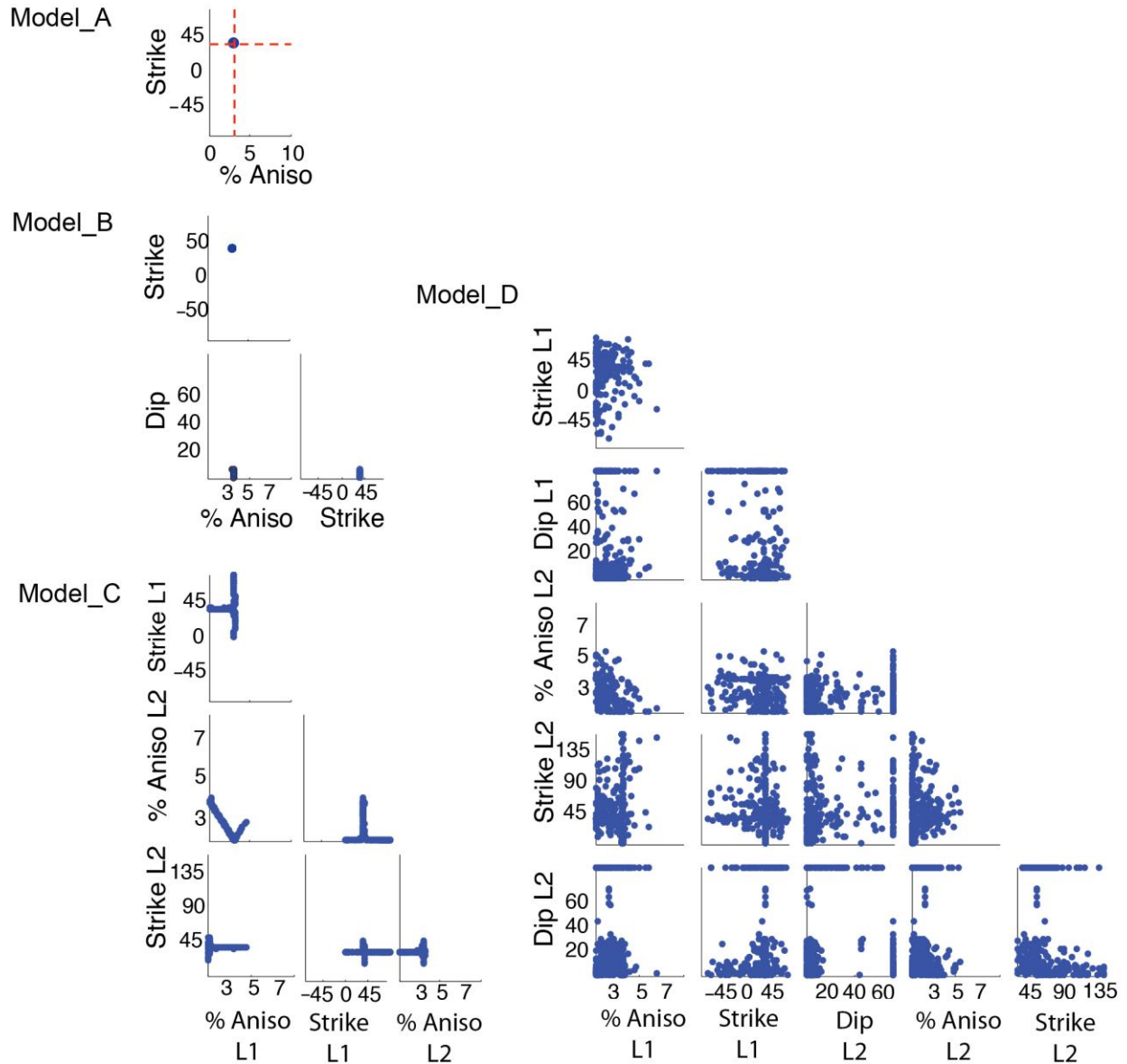


**Figure 16.** 2-D bootstrap distributions for FFC\_SD\_A. Each subplot is labeled by the model parameterization. The model parameter names and values are labeled along the bottom and left sides of the matrices. Strike is rendered in degrees positive clockwise with respect to North, and dip is rendered in degrees positive downward from horizontal. For the *properly parameterized* model (A), values for the input parameters used to generate the synthetic data are shown by red dashed lines.

1- and 2-D bootstrap results from testing of FFC\_SD\_D are shown in **figures 17 and 18**, respectively. The 1-D distributions show that all *under-parameterized* models (A, B, C) are able to resolve the upper layer input parameterizations, with the exception that model B fails to resolve the

input for upper layer dip. The 2-D distributions for model B show that while solutions for % anisotropy and strike are uni-modal, solutions for dip are distinctly tri-modal converging on either  $0^\circ$ ,  $90^\circ$ , or  $\sim 30^\circ$ . Interestingly, this multi-modality of the dip solution, with little correlation to % anisotropy or strike for model B, also appears in the bootstrap and PDF results for the model B parameterization of the real data set (**figure 15**). The model C 1-D distributions show proper resolution of both input parameters for the upper layer and % anisotropy in the bottom layer, but the model has difficulty resolving bottom layer strike. Model C distributions also show a distinct multi-modality. Solutions for the *properly-parameterized* model (D) all show proper resolution of the input parameters, and generally appear to be uni-modal in the 1-D distributions, with the exception of bottom layer strike and dip. Inspection of the 2-D distributions reveals that solutions are non-unique, but highly clustered around the input parameters, with little clustering elsewhere.

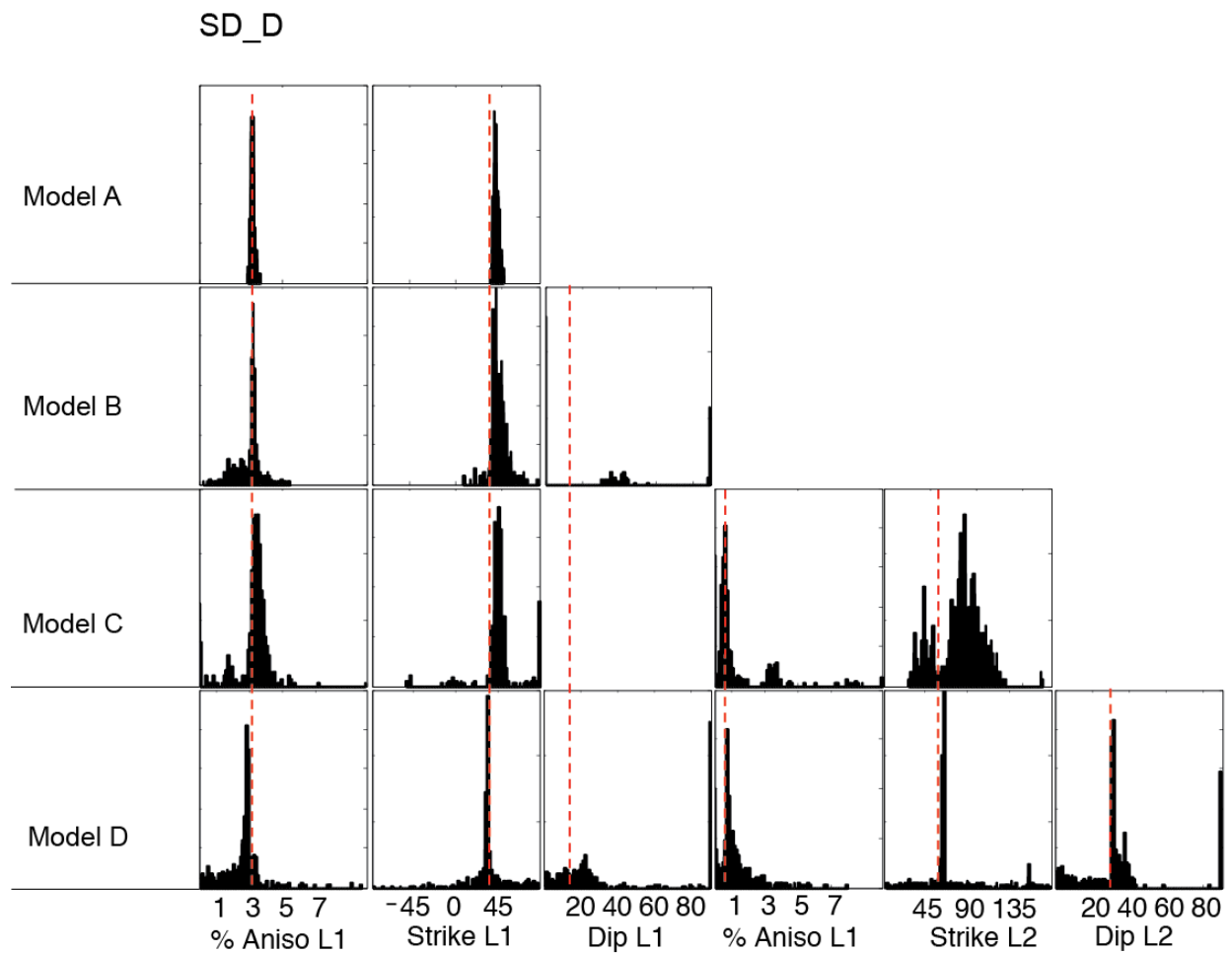


**Figure 17.** 1-D bootstrap marginals for FFC-SD\_D-synthetics. See **Figure 15** for figure layout description. The red dashed lines represent values of input parameters used to generate FFC\_SD\_D.

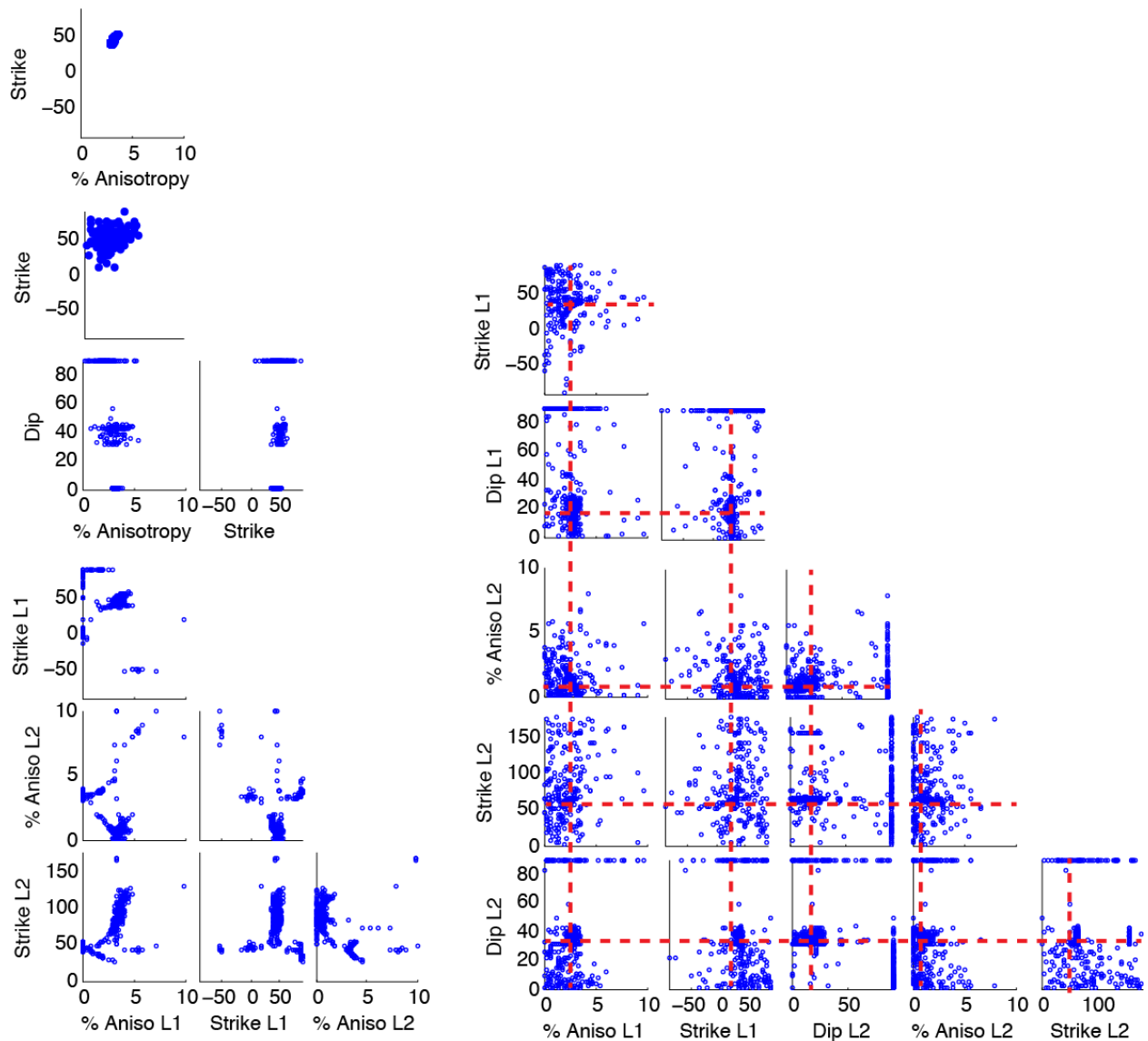


**Figure 18.** 2-D bootstrap marginals for FFC\_SD\_D-synthetics. See **Figure 16** for figure layout description. For the *properly parameterized* model (D), values for input parameters used to generate the synthetic data are shown by red dashed lines.

#### 2.4.2.4 Summary of results at FFC

To summarize, we find that the uneven back azimuthal distribution of events introduces a bias into the FFC data set that has an effect on our solutions, and we therefore choose to weight the data set. We find that a single layer solution with a FVA strike at  $\sim 40^\circ$  and  $\sim 3\%$  anisotropy is stable across all four parameterizations, with both two layer models finding that solution in an

upper layer, and allowing for dip does not appear to alter that solution. The lower layer solution is less stable between models, and does appear to depend on dip. None of our reduced models (A, B, and C) can be rejected against the full model (D) with 2-sigma confidence, but at 1-sigma confidence we can reject models A and B, and fail to reject model C. Therefore, allowing for two layers to dip in model D does not provide a significantly better fit to the data than a two flat layer model. Synthetic testing shows that both our simplest (model A) and most complex (model D) solutions produce the same stable upper layer solution seen in results from the real data. But, the synthetics also show that the lower layer solution for a flat FVA parameterization is not well constrained in the presence of a dipping FVA, contrary to what was seen from testing the real FFC data set.

### **2.4.3 RSSD**

#### *2.4.3.1 Best fitting solutions*

Individual best-fitting parameter results and associated confidence intervals are presented in **table 4**. 95% confidence intervals for % anisotropy and strike for the two dipping models (B and C) span more than 50% of the parameter space in most cases. This observation is also reflected in the 1- and 2-D marginal distributions (**figures 19 and 20**) where solutions are wide, multi-modal, and irregularly shaped. These results show that dipping models are not resolvable by our data set.

Solutions for the non-dipping models (A and C) are reasonably constrained, with relatively tight and uni-modal marginal distributions. However, individual parameter solutions show no overlap between the two models. Model A places very little anisotropy (less than 1%) in a layer striking  $\sim 60^\circ$  from North, while model C places large and equal amounts of anisotropy ( $\sim 6.5\%$ ) in two layers with nearly perpendicular strikes, neither of which correspond to the model A strike. An F-test comparing models A and C (**figure 21**) shows that the rejection probability for model A is

56%, and therefore we cannot reject the null hypothesis that model C provides a significantly better fit to the data.

**Table 4: Model results for RSSD data set.**

<b>Model</b>	<b>A</b>	<b>B</b>	<b>C</b>	<b>D</b>
<b>% Anisotropy Layer 1</b>	0.73 [0.63, 0.90]	6.73 [2.36, 7.84]	6.73 [6.03, 7.04]	0.00 [0.00, 7.64]
<b>Strike Layer 1</b>	-58.87 [-62.48, -54.36]	-31.21 [-90, -12.21]	27.59 [15.83, 36.63]	45.68 [-90.00, 71.01]
<b>Dip Layer 1</b>		90 [85.93, 90.00]		90.00 [81.86, 90.00]
<b>% Anisotropy Layer 2</b>			6.53 [5.88, 7.14]	3.47 [1.41, 5.78]
<b>Strike Layer 2</b>			117.59 [108.54, 135.68]	44.32 [7.24, 86.83]
<b>Dip Layer 2</b>				29.40 [6.78, 41.61]
<b>Degrees of Freedom</b>	375	374	373	371
<b>Chi-Squared</b>	17.1	N.A.N.	17.0	N.A.N.

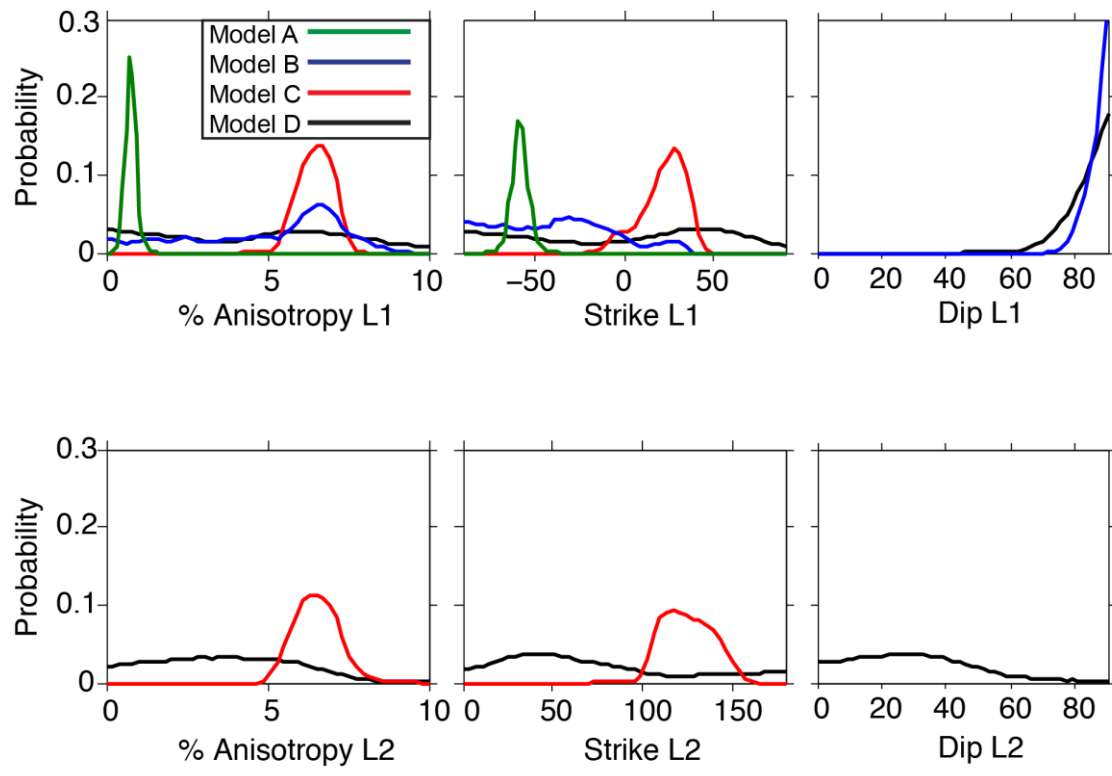


**Figure 19.** 1-D PDF marginals for RSSD data set. See **Figure 12** for figure layout description.

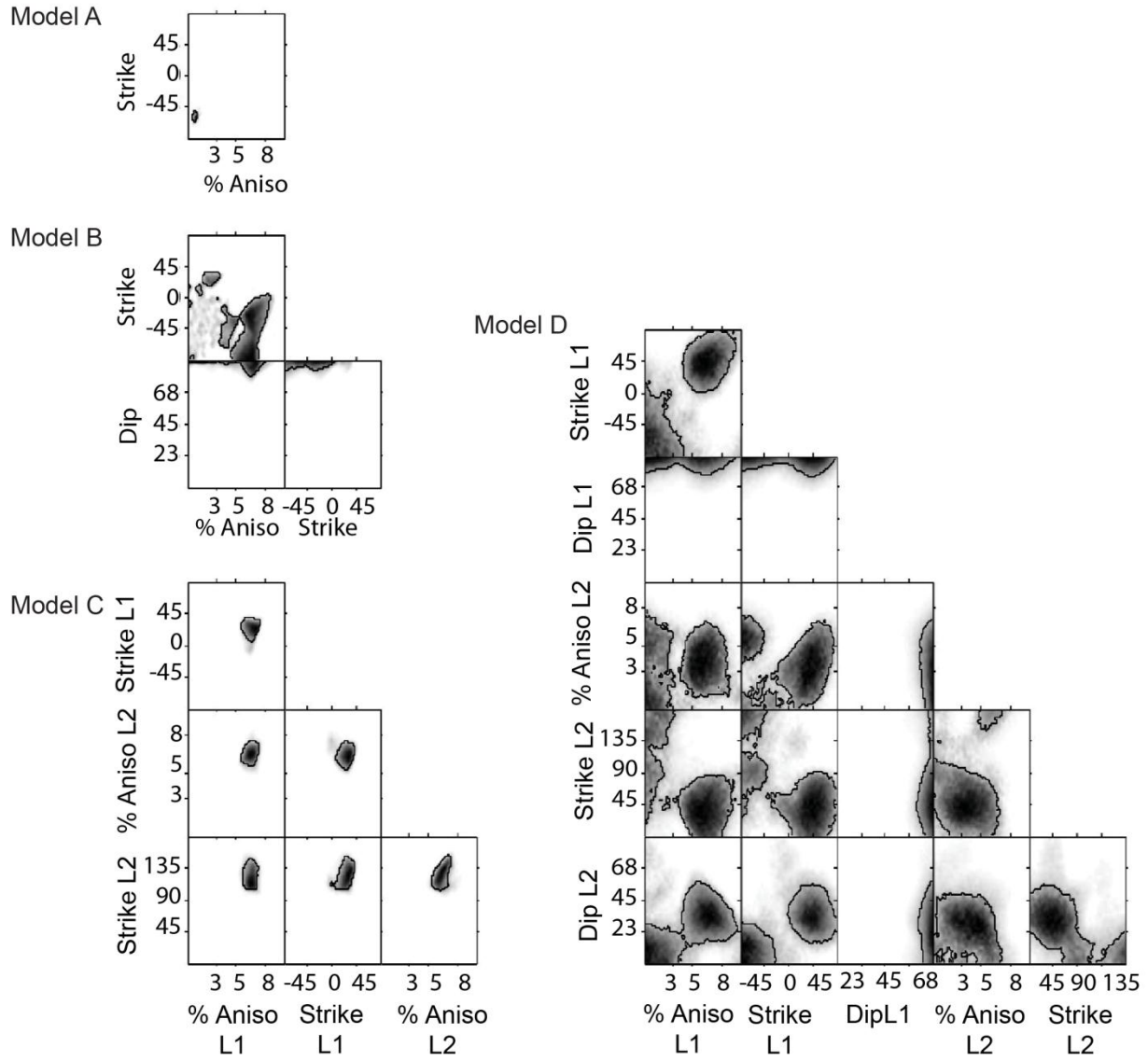


**Figure 20.** 2-D PDF marginals for RSSD data set. See **figure 13** for figure layout descriptio

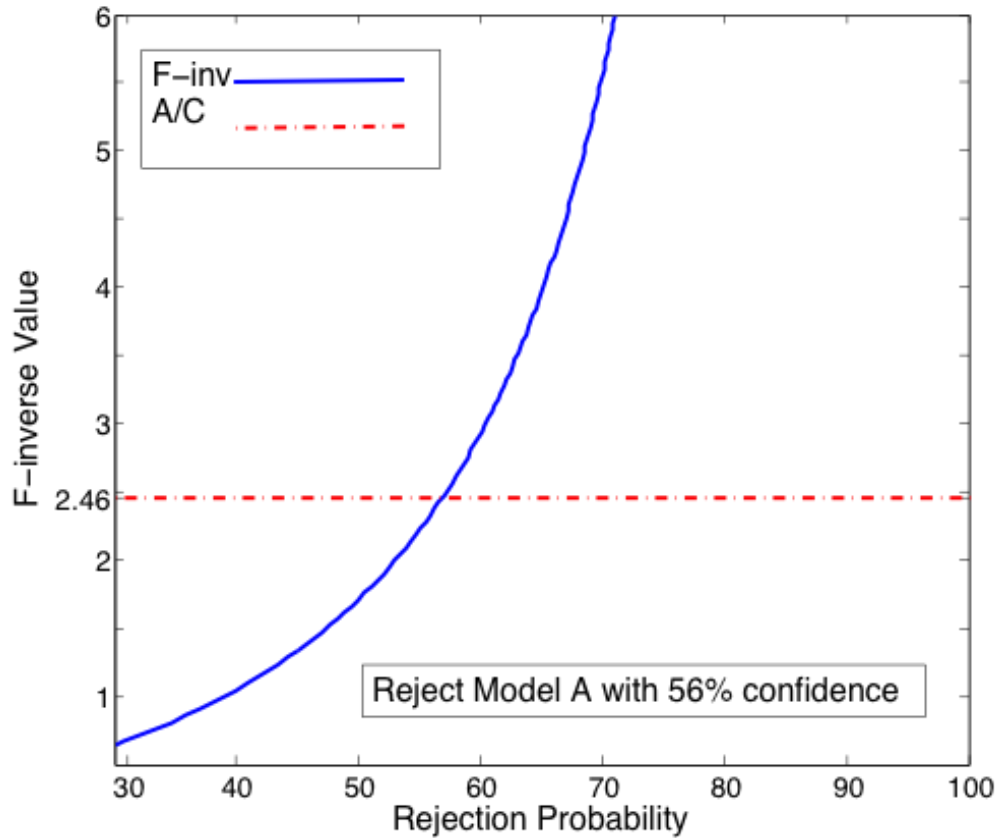


**Figure 21.** F-test for comparing models A and C results for RSSD data.

#### 2.4.3.2 Bootstrap Analysis

A bootstrap analysis of the full data set was conducted and 1- and 2-D distributions are shown in **figures 22** and **23**, respectively. Unlike the PDF marginals, the bootstrap distributions show a wide variety of solutions for models A and C, suggesting the PDF calculations may underestimate the true uncertainty.

Several studies have shown that in the presence of two or more anisotropic layers, single layer solutions will display a systematic variation of ASP with back azimuth [*Silver and Savage, 1994; Liu et al., 1995; Silver 1996; Snyder et al., 2007; Silver and Long, 2010*]. Apparent splitting

parameters found by analyzing RSSD data using the Silver and Chan method (**figure 10**), show clear variations in both delay time and fast axis orientation that are inconsistent with a single layer of homogeneous anisotropy. Given that a two layer model does not fit the data significantly better, it stands to reason that there is lateral heterogeneity of anisotropic structure under RSSD, and different rays are sampling different anisotropy. This would explain the diffuse results of the bootstrapping runs.

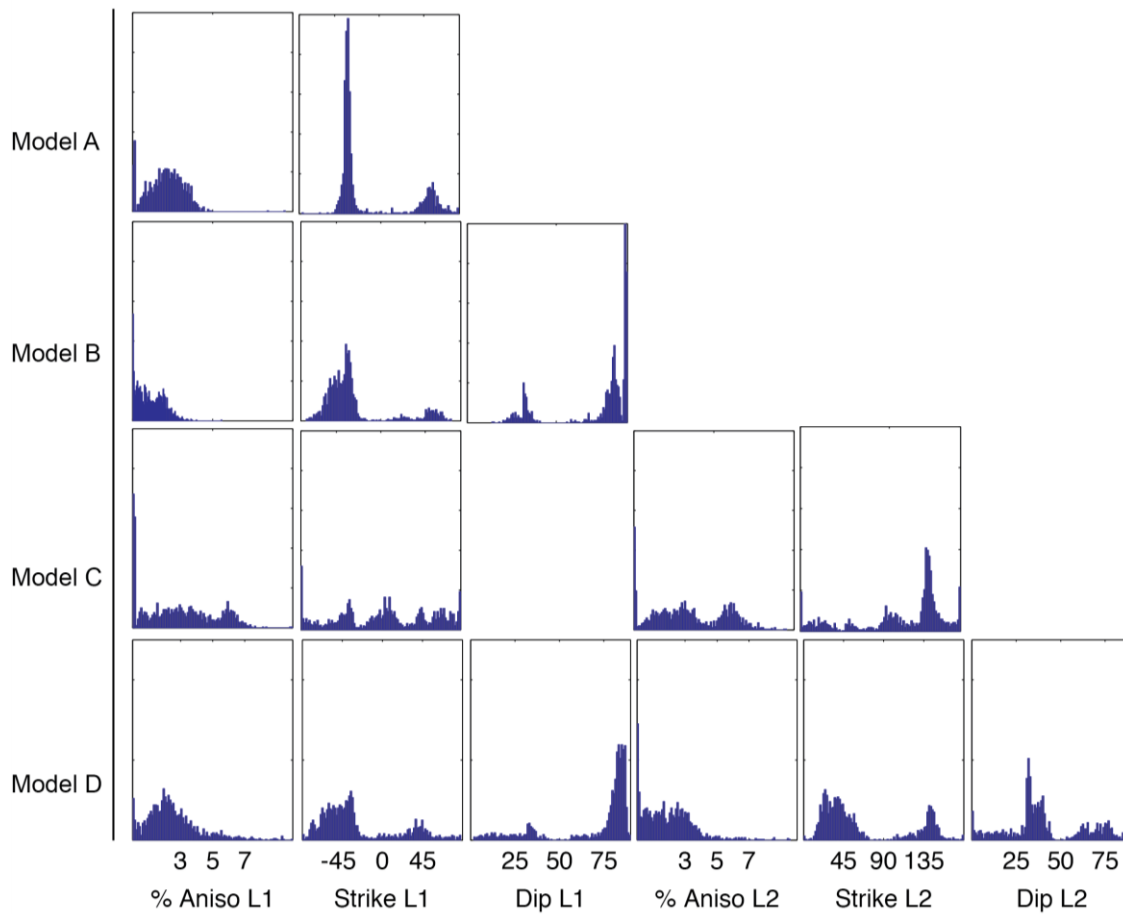


**Figure 22.** 1-D bootstrap distributions for RSSD data set. See **figure 15** for figure layout description.

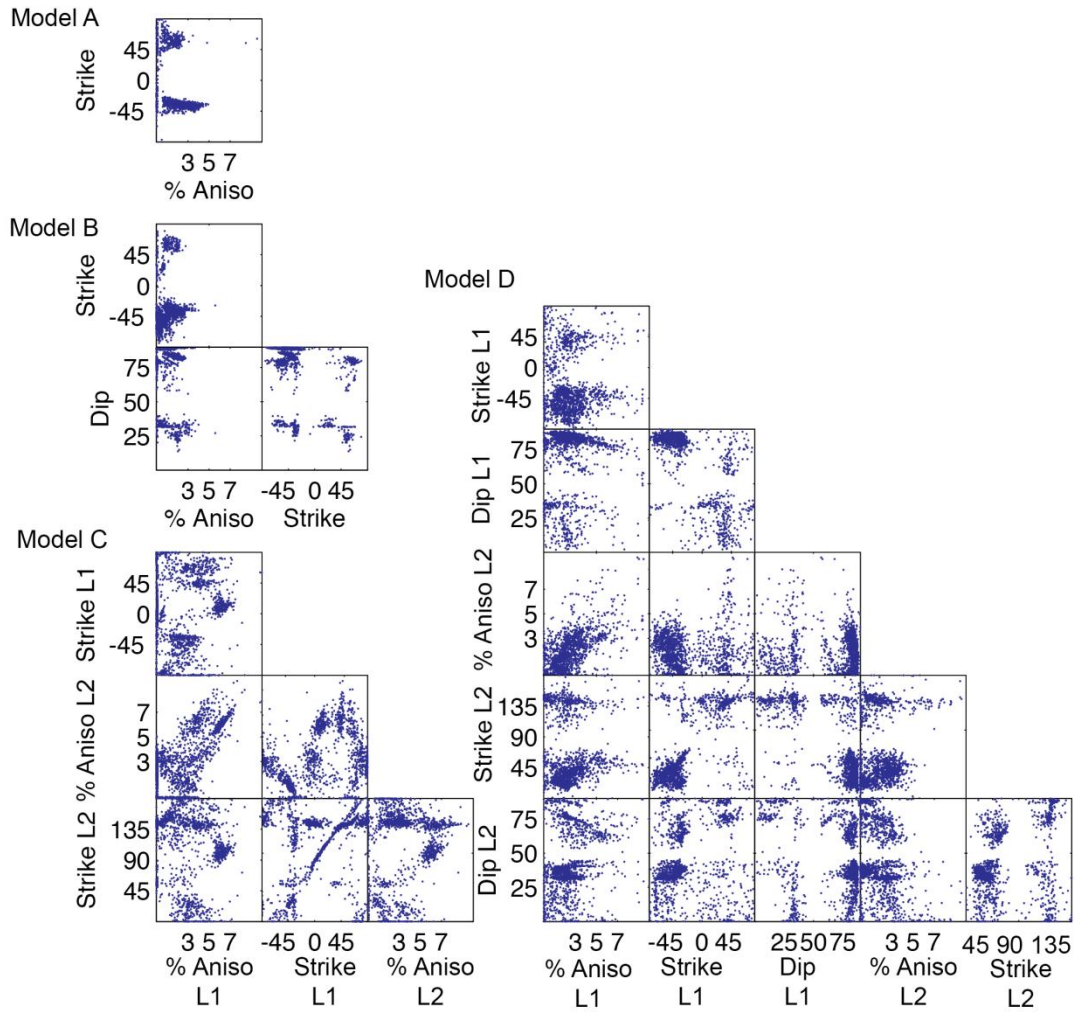


**Figure 23.** 2-D bootstrap distributions for RSSD data set. See **figure 16** for figure layout description.

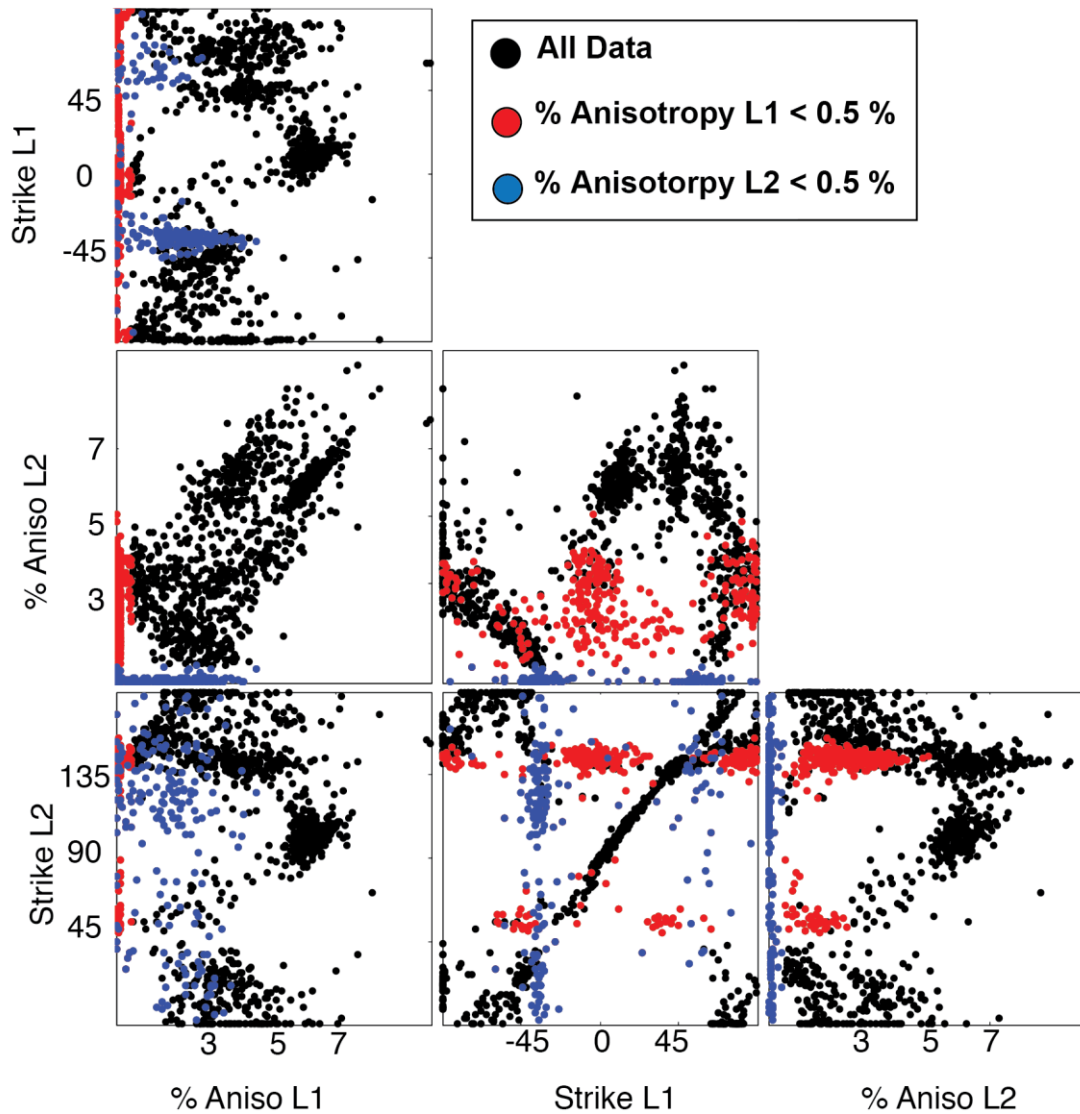


**Figure 24.** 2-D model C bootstrap distributions for RSSD data set (black) showing solutions in which the upper layer (red) or lower layer (blue) contains < 0.5% anisotropy.

Bootstrap distributions for model C reveal a variety of linear trends that indicate covariance between model parameters (**figure 24**). The most significant of these are seen in the Strike L1 vs. Strike L2 distribution, where trends with a slope of indicated that the model found no anisotropy in the upper layer, trends with a vertical slope indicate that the model found no anisotropy in the lower layer, and trends with a slope of one indicate that the model found anisotropy

perpendicularly striking anisotropy between the two layers, along which the best fitting solution for model C lies.

### 2.4.3.3 Synthetic Testing

To investigate whether the patterns in the bootstrapping results for RSSD are due to the limited back azimuthal range of events we bootstrap synthetic datasets. Two synthetic data sets, RSSD\_SD\_A and RSSD\_SD\_C, are generated based on anisotropic geometries from the best fitting solutions from **table 4** for models A and C, respectively. The synthetic data sets were generated in the same manner as those from FFC (**see section 3.2.4**). Best fitting solutions along with input parameters for both data sets are shown in **tables 5** and **6**. For RSSD\_SD\_A, both single layer models properly resolved the input parameters, and model B only allowed for a 5° dip. Both 2-layer models successfully resolved the input parameters in one of the two layers, and only allowed for 0.1% anisotropy in the other layer: For RSSD\_SD\_C, the best fitting solutions for model C underestimate % anisotropy in both layers, and strike of the bottom layer ~15° off.

**Table 5: Best fitting solutions for RSSD\_SD\_A**

Model	Aniso L1	Strike L1	Dip L1	Aniso L2	Strike L2	Dip L2
<b>INPUT</b>	<b>0.73</b>	<b>-58.9</b>				
A	0.8	-58				
B	0.8	-58	5			
C	0.1	3		0.8	121	
D	0.8	-61	9	0.1	144	21

**Table: 6: Best fitting solutions for RSSD\_SD\_C**

Model	Aniso L1	Strike L1	Dip L1	Aniso L2	Strike L2	Dip L2
<b>INPUT</b>	<b>6.73</b>	<b>27.69</b>		<b>6.53</b>	<b>117.59</b>	
A	2	70				
B	2	70	17			
C	5.8	27		6.1	101	
D	5.9	25	10	5.9	99	12

Bootstrap distributions for both synthetic data sets are compared to those of the real data set in **figure 25**. The figure shows *properly-parameterized* models are capable of resolving the input parameters, indicating that data coverage is indeed sufficient to resolve one or two layer structure. By comparing the distributions of the synthetic data sets to those of the real data set, we see that neither synthetic data set can fully explain the real data, providing further evidence that anisotropic heterogeneity explains the observations at RSSD.

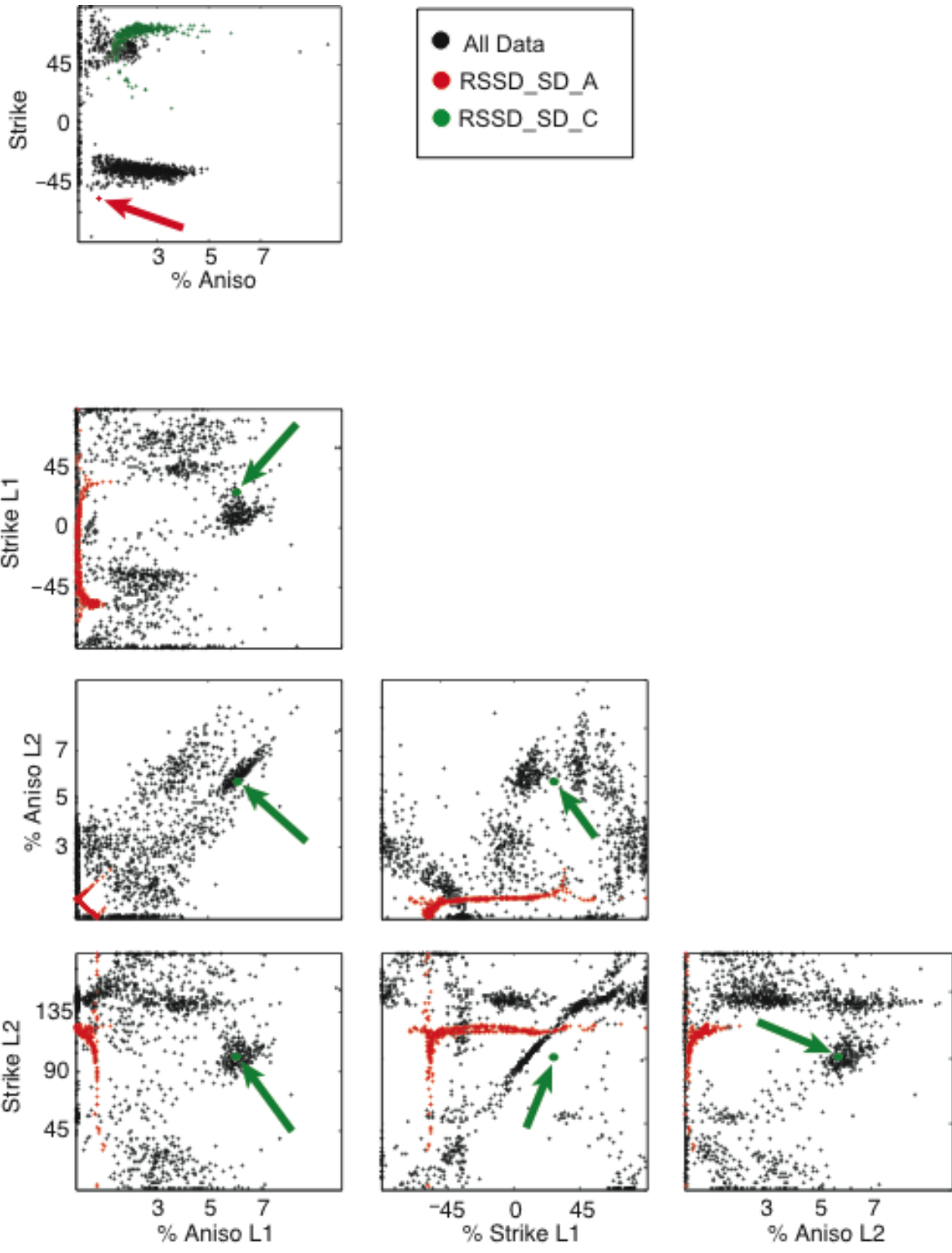


**Figure 25.** Models A and C 2-D bootstrap distributions for the true RSSD data set (black), RSSD\_SD\_A (red), and RSSD\_SDC (green).

#### 2.4.3.4 Summary of results at RSSD

To summarize, we find one and two flat layer model solutions for RSSD that appear to resolve different anisotropic geometries, we cannot determine which model can statistically explain the data better than the other. Synthetic testing indicates that the data distribution should be capable of resolving both a one and two flat layer anisotropic geometry.

## 2.5 Discussion

### 2.5.1 FFC

Results for FFC show that a model with two flat layers of anisotropy (model C) can properly account for the data. We therefore interpret the anisotropy beneath FFC in the context of two flat layers, with 2.9% anisotropy striking  $\sim 38^\circ$  in an upper layer, and 1.2% anisotropy striking  $\sim 74^\circ$  in a lower layer. The lower layer strike is subparallel to absolute plate motion (APM) oriented at  $\sim 62^\circ$  clockwise from north according to the HS3-NUVEL1A model [Gripp and Gordon, 2002] (**figure 26**). Anisotropy in this lower layer (at a depth greater than 140 km) is most likely caused by shear in the asthenosphere due to absolute plate motion [Yuan *et al.*, 2011].

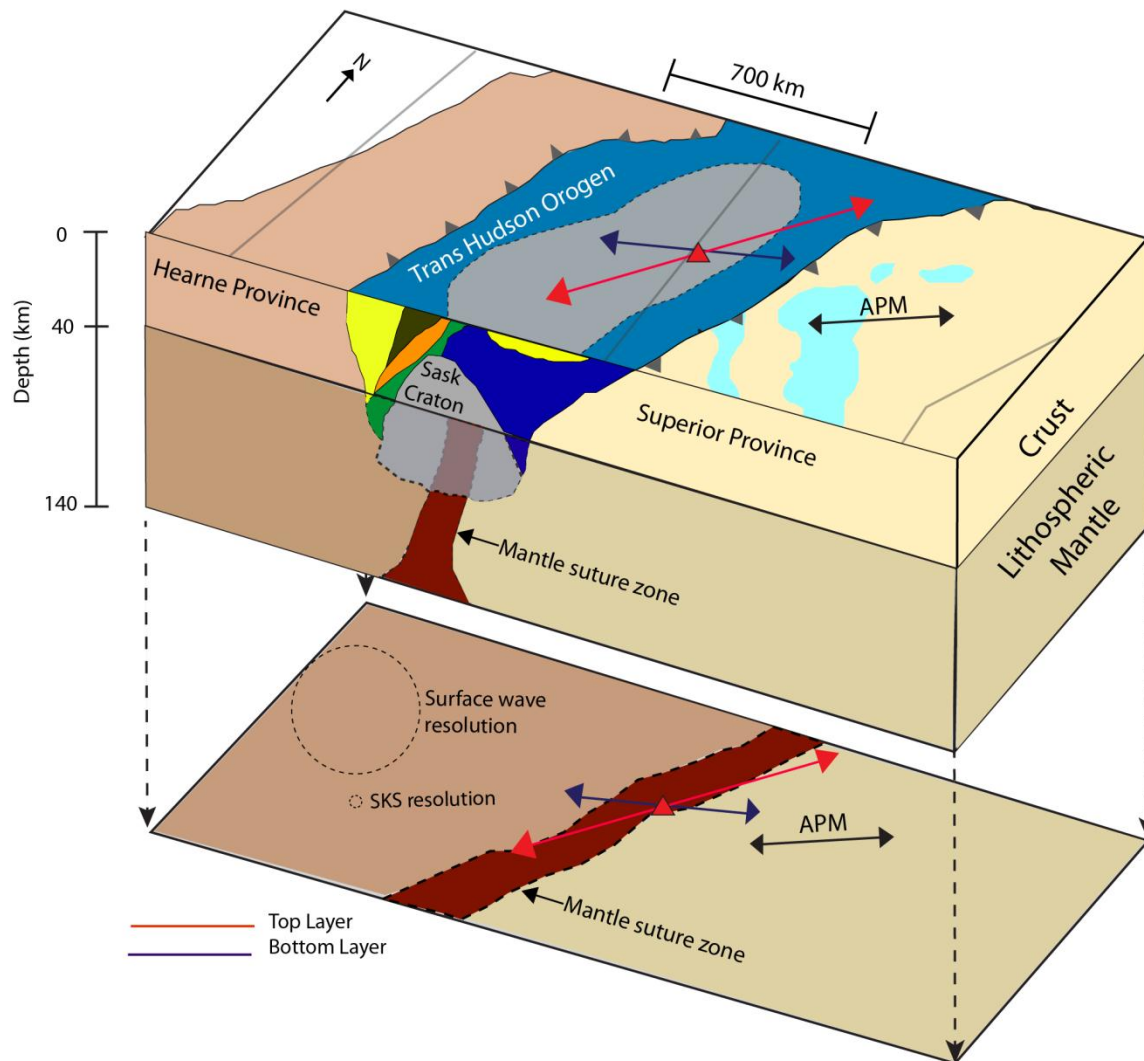


**Figure 26.** Interpretation of anisotropy at FFC. The location of FFC is marked by a red triangle in both the upper and lower parts of the figure. The upper block portrays the tectonic setting as described in **figure 5**. In cross section, mantle dynamics at the time of collision as hypothesized from seismic reflection data by *Nemeth et al.* [2005] are shown. The buried Sask craton is surrounded by various accreted terrain fragments. The extent to which these terrains extend into the mantle lithosphere is not known, nor is the extent to which Sask lithospheric mantle is preserved. Our interpretation of dynamics at the base of the lithosphere is projected onto the lower plane. Orientations of absolute plate motion (black arrow), strike FVA of the top layer (red arrow), and strike FVA of the bottom layer (blue arrow) are all shown. The strike of the bottom layer found by this study is sub-parallel to APM, and the strike of the upper layer is oriented sub-parallel to the mantle suture zone.

The most prominent feature of our model is a strongly anisotropic ( $\sim 3\%$ ), NE striking, upper layer, which we interpret to represent lithospheric anisotropy inherited from craton forming

events. This upper layer strike is sub-parallel to the hypothesized mantle suture zone, proposed by *Nemeth et al.* [2005], that is the structural manifestation of the final events of the Trans Hudson Orogeny. Using a joint surface wave-SKS inversion model (SAWum\_NA2) *Yuan et al.* [2011] found multiple layers of anisotropy beneath FFC (**figure 27**). The uppermost layer in their model correlates well with our upper layer result, but is underlain by a laterally continuous layer striking  $\sim -90^\circ$ , that is not present in our model. Global models of seismic anisotropy often contain regions that are sampled poorly, necessitating that the entire model be smoothed strongly [*Becker et al.*, 2012]. The lateral resolution of the SAWum\_NA2 model is limited to  $\sim 500$  km. Because lateral resolution in this study is determined by the width of the Fresnel-zone for a typical SKS, our method has a lateral resolution that is less than 40 km [*Silver and Chan*, 1991], and is sensitive to smaller scale structures that are smoothed over in other inversions. Therefore our model may present a more accurate representation of the anisotropic structure beneath FFC. Furthermore, the stability and tight constraint of the upper layer solution imply that this fabric is coherent on the resolution scale of this study.

The upper layer found in this study implies that Trans Hudson Orogeny deformation extended down into lithosphere, which underwent a high degree of reworking, resulting in a strong anisotropic fabric that has either erased or highly obscured any preexisting fabrics, and remained stable ever since.

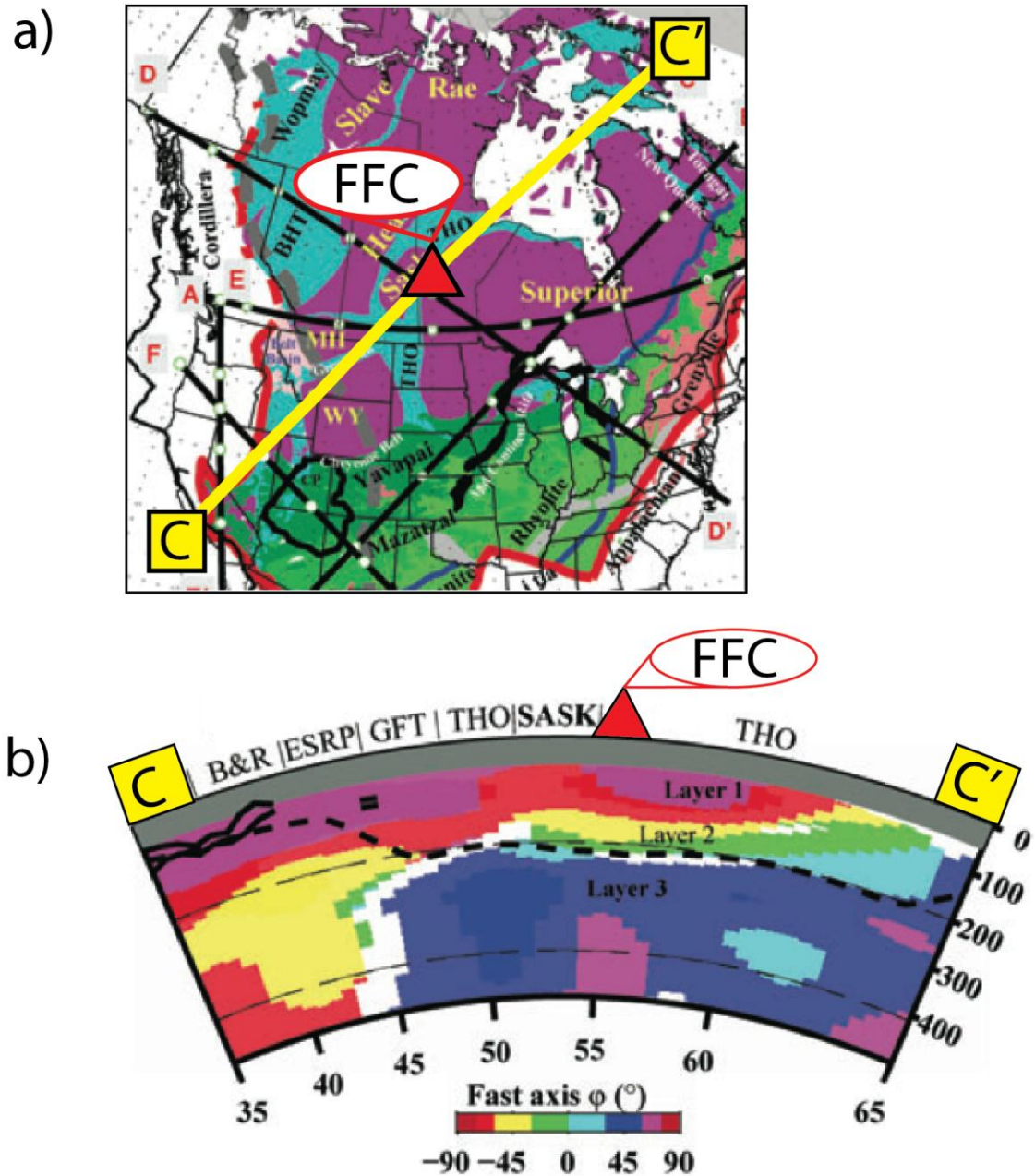


**Figure 27.** Joint surface wave-SKS inversion results for a SW-NE transect across the THO. (a) Map view of transect. FFC is located along the C-C' transect. (b) Cross-section view of azimuthal anisotropy along the C-C' transect. The black dashed line is the interpreted lithosphere-asthenosphere boundary. The significant increase in depth of this boundary beneath the Great Falls Tectonic Zone (GFT) represents the transition into the craton. The color bar shows the orientation of the fast velocity axis. The model shows three distinct layers of anisotropy beneath FFC [Yuan *et al.*, 2011].

The stability of the upper layer solution across all four model parameterizations has significant implications for how SWS data is interpreted. While not exactly parallel to plate motion, the strike of this layer, along with its significant amount of anisotropy, may cause it to be mistakenly interpreted to represent plate motion shear in a single layer context. However, by employing a two layer model, it becomes clear that the single layer solution instead correlates with the upper-most of two layers, and is likely a significant structural feature in the lithosphere, while shear due to plate motion contributes minimally to the observed anisotropy in a single layer model.

### **2.5.2 RSSD**

At RSSD, the one layer model (A) solution is distinctly different from the two layer model (C) solution, and we cannot statistically determine which model provides a better fit to the data. At the same time, when analyzed with the *Silver and Chan* [1991] method, RSSD data produced significant variations in apparent splitting parameters for rays from similar back azimuths, suggesting either unusual signal-generated noise or anisotropic heterogeneity at roughly SKS wavelength scales.

Using the *Silver and Chan* [1991] method, two previous studies identified a strong discrepancy in shear wave splitting results across the THO (**figure 28**) [*Silver and Chan*, 1991; *Silver and Kaneshima*, 1993], which they attribute to lateral heterogeneity on the scale of 1000 km. These studies found a FVA of  $55^\circ$  and a delay time of 0.65 second for RSSD, corresponding almost perfectly to our model A result. As absolute plate motion at RSSD is  $\sim 69^\circ$  [*Gripp and Gordon*, 2002]. This FVA direction would seem to support a single layer hypothesis where shear due to plate motion leads to the development of lattice preferred orientation of olivine in the asthenosphere, and is the primary contributor to shear wave splitting observations of anisotropy [*Vinnik et al.*, 1992]. But as these early studies recognized, if plate motion were the sole contributor to anisotropy, shear wave splitting results should not display significant variation on a regional scale.

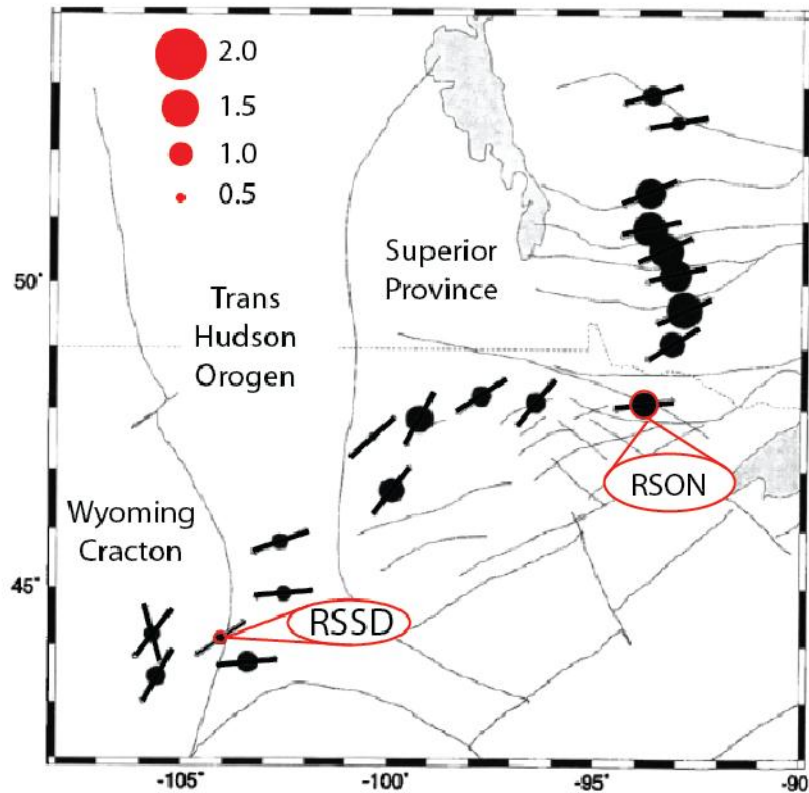


**Figure 28.** SWS results from *Silver and Chan [1991]*. Results are plotted at station locations. Circle radius is proportional to split time and lines are plotted in the orientation of FVA strike. A strong discrepancy is noted in both delay time and FVA strike between stations RSSD and RSON.

Geological evidence exists for two lithospheric layers. Exposure of basement rocks in the Black Hills reveal two dominant structural fabrics: A NE-SW fabric is attributed to Archean deformation, and a NW-SE fabric is attributed to the Proterozoic THO deformation events [*Dewitt et al., 1986; Gosselin et al., 1998*]. *Silver and Chan [1991]* hypothesized that these two nearly perpendicular fabrics were the primary contributors to anisotropy, and effectively cancelled each other out, resulting in the low split times observed at RSSD. The two FVAs found by model C would appear to support this hypothesis, but our synthetic results show that this geometry does not produce the low delay times found under the single layer assumption.

While our results for RSSD appear to support geological predictions for both a one and two layer case, we've shown that neither model alone can account for the data, which in conjunction

with the lack of back-azimuthal dependence leads us to hypothesize that inconsistencies in our results may be caused by lateral heterogeneity beneath RSSD. Because the width of the Fresnel-zone for a typical SKS wave is  $\sim 40$  km [Becker, 2012], this would indicate that heterogeneity occurs on a scale an order of magnitude less than that originally hypothesized by *Silver and Chan* [1991]. A shear wave splitting study of cratonic northwestern Canada identified anomalous splitting characterized by small delay times at stations adjacent to an ancient suture zone, hypothesizing that that small-scale structures on a length scale of  $\sim 100$  km noticeably affect shear wave splitting measurements, and are responsible for the anomaly [Courtier *et al.*, 2010]. They further hypothesize that these small delay times result from a dipping structure associated with paleosubduction. Located on the margin of the Wyoming craton and adjacent to the THO, RSSD exhibits similar anomalously small delay times. However, our results show that this reduction in this small delay time does not result from the presence of a single dipping structure, as tested in model B. Instead, we interpret this anomalous splitting in proximity to ancient suture zones to be the result of small-scale anisotropic heterogeneities.

## 2.6 Conclusions

In this study we've presented two cases for which SKS data from the THO feature is examined in a multiple layer context. For station FFC, we resolved a two layer structure and interpreted that tectonic deformation in the lithosphere relating to the continent forming events of the Trans Hudson Orogeny is the primary contributor to anisotropy in the area, while shear due to plate motion contributes less. The stability of the upper layer solution across all four of our tested models strongly suggests that the associated fabric is coherent on the resolution level of SKS waves, and that heterogeneity on a smaller scale is either obscured by this fabric or absent all together. When analyzed under the single layer assumption, the signal due to plate motion shear is entirely obscured in favor of the lithospheric signal. Because our two layer model shows that both layers

strike within 25° of absolute plate motion, the one layer solution can be easily misinterpreted to represent plate motion shear, and all information carried in the lithospheric solution would be lost. This observation reinforces the need for cratonic SKS data to be examined in a multiple layer context such as that presented in this study.

For RSSD, we were unable to resolve a specific anisotropic structure, but we diagnosed lateral heterogeneity on a scale smaller than 40km. Previous studies had identified lateral heterogeneities on a scale of 1000 km, but here we show that anisotropy can vary on a scale an order of magnitude less. As it would be hard to imagine non-subduction related mantle flow varying over such a small scale, we conclude that the heterogeneity beneath RSSD results from imbricated anisotropic fabric in the lithosphere formed during the Trans Hudson Orogeny.

Results from both FFC and RSSD suggest that fabrics formed during craton amalgamation are stable and remain preserved in the lithosphere today. However they also suggest that there exists a disparity in lithospheric formation mechanics between the station locations. The crustal expression of continental collision is a wide orogenic belt, but in the stronger lithospheric mantle, the suture forms a more narrow zone located in the center of the orogenic belt [*Davies and von Blackenburg, 1995; Nemeth et al., 2005*], where tectonically induced strain weakening leads to plastic flow that creates anisotropic fabric aligned parallel to the suture. The strength, orientation, and lateral continuity within less than 40 km of our upper layer solution for FFC strongly supports this model and suggests that FFC is located directly above the mantle suture zone. RSSD however, shows no coherent suture-oriented anisotropy. While the exact southern extent of the Trans Hudson Orogen is poorly known, rock outcrops in the Black Hills definitively place RSSD within the Trans Hudson zone [*Dahl et al., 1999*]. The simplest explanation for the lack of suture-oriented anisotropy in this location is that SKS data from RSSD does not sample the narrow Trans Hudson mantle suture. We hypothesize that the mechanics of continental collision outside of that zone fail

to develop coherent fabrics, and the lithosphere instead contains small fragments that cause anisotropic heterogeneity.

The anisotropic identification of a narrow lithospheric-mantle suture zone at FFC would not have been possible without a multiple layer approach to analyzing SKS data. Beyond identifying this zone, the approach used in this study may provide a means to definitively trace the Trans Hudson Orogen throughout the North American continent using SKS data. Conversely, the identification of anisotropic lateral heterogeneity on scales less than 40 km at RSSD raises questions on how the mantle lithosphere is accommodated during convergence away from the suture zone. Further studies of SKS data from the Trans Hudson zone are needed to address these questions, but in this study we've shown that examining SKS data in a multiple layer context provides the means.

## Chapter 3

### PROCESSING AND RECCOMENDATIONS

#### 3.1 Overview of Processing

##### *3.1.1 Data acquisition*

The basic processing stream used for this project is shown in **figure 29**. Data is electronically requested via an xml formatted file that is sent to the Incorporated Research Institutes for Seismology Data Management Center (IRIS\_DMC). The file is generated using the Standing Order for Data website [<http://www.seis.sc.edu/sod/>] (see **appendix A** for SOD recipe). Beyond retrieving the data, the SOD recipe also formats the data into Seismic Analysis Code (SAC) [*Goldstein et al., 2003; Goldstein and Snoke, 2005*] file format, and picks the SKS arrival using TauP travel time calculator [*Crotwell et al., 1999*].

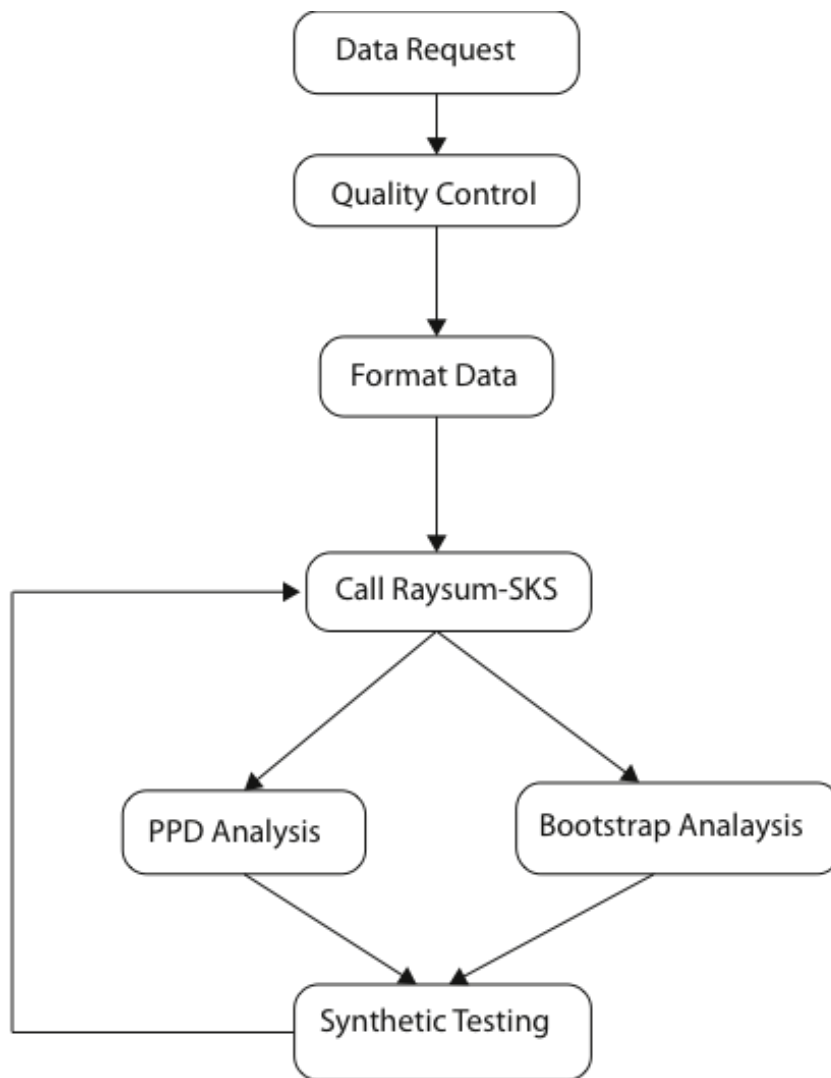


**Figure 29.** Basic processing stream.

### ***3.1.2 Quality control and data formatting***

The quality control process includes both automated and non-automated steps (see **figure 30**). Automated processes included checking the signal to noise ratio, and checking for other arrivals (such as SKKS) within close proximity to the SKS pick. Beyond these steps, a visual inspection of the waveforms is still required. Waveforms that pass the criteria discussed above can exhibit attributes that are difficult to define. For example, in **figure 31** the waveform has a high

signal to noise ratio and no other arrivals are present, but a low frequency signal is seen arriving after the SKS pick that would certainly effect the measurement.

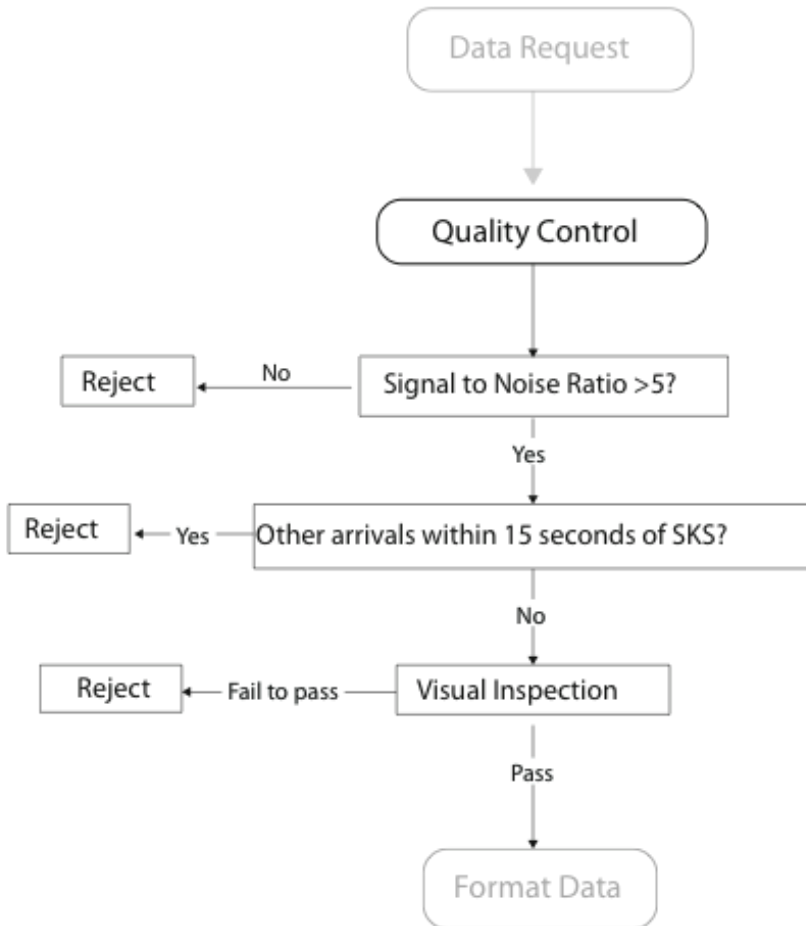


**Figure 30.** Quality control processing stream.

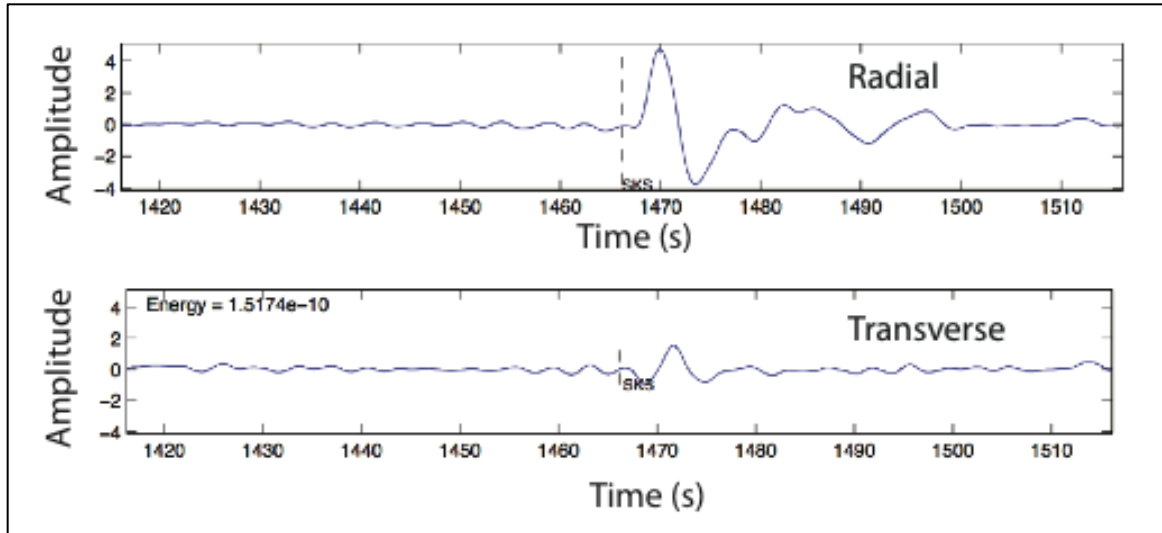


**Figure 31.** Example waveform that would fail visual inspection. While the signal to noise ratio is high, and no other arrivals are present, there is a low frequency signal that follows the SKS signal.

In order to properly format the data, a ‘splitting window’ must be defined. This window will contain the piece of the waveform that is to be analyzed. For large quantities of data, the simplest way to set this window is to define it as 5 seconds prior to and 20 seconds after the predicted SKS arrival using the PREM model [Dziewonski and Anderson, 1981]. While generally appropriate (see **figure 32a**) there are times when the predicted and true SKS arrivals do not agree. In this case, the automatic window can cut off part of the SKS signal (see **figure 32b**). This issue again leads to a need for visual inspection. In this study, the SKS window was automatically selected from the predicted arrival and visually inspected, but new approaches that more effectively automate this process will greatly reduce processing time in the future.

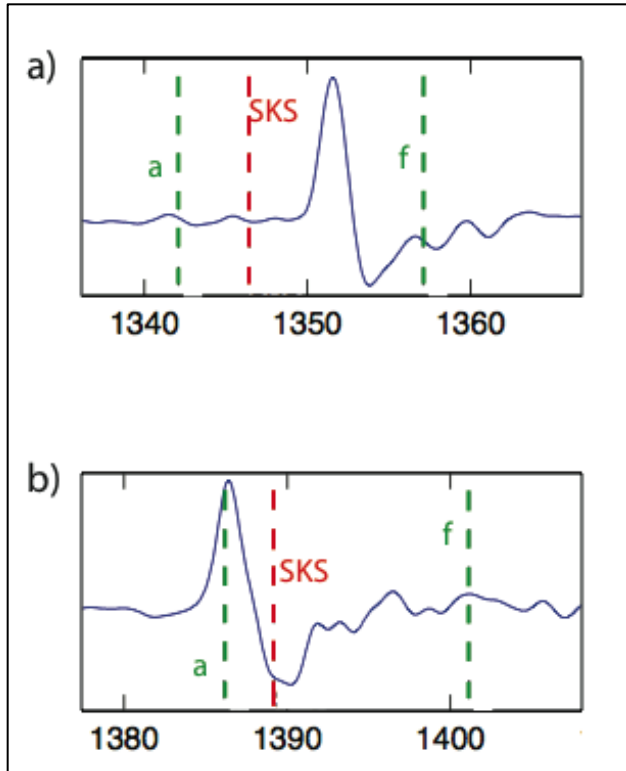


**Figure 32.** Demonstration of automatic window selection. The splitting window is marked by the headers a and f. **a)** The predicted arrival time corresponds well with the SKS energy arrival, and the automatic window captures all of the SKS energy. **b)** The SKS energy arrives before the predicted arrival time, and the automatic window truncates a significant portion of the real signal.

Once the window is selected, a 10 seconds long slice of the trace arriving before the onset of the splitting window is used to define the level of the noise. The SAC files are read into Matlab, and the waveform error is taken from the signal to noise ratio, calculated by taking the root mean-square (RMS) amplitude of the noise trace, and dividing it by the RMS of the signal.

### 3.1.3 Running Raysum

The core of the processing is performed by the program Raysum\_SKS, which calls the Neighborhood Algorithm to search the parameter space and return an ensemble of best fitting models. Raysum\_SKS was written by Huiyu Yuan who granted this study full permission to use and modify it, and will be a co-author on the resulting paper. The package itself is written in Fortran,

but we opted to control the work-flow in Matlab, as laid out in **figure 33**. The basic flow is designed to analyze SKS data that has been properly formatted and organized into individual station directories. After the data is read in, the model parameterization is selected and Raysum\_SKS is called. Raysum returns numerous output files including a list of all models found and there corresponding errors, the best fitting model, and a file containing all of the information generated by the search that is used for statistical analysis.

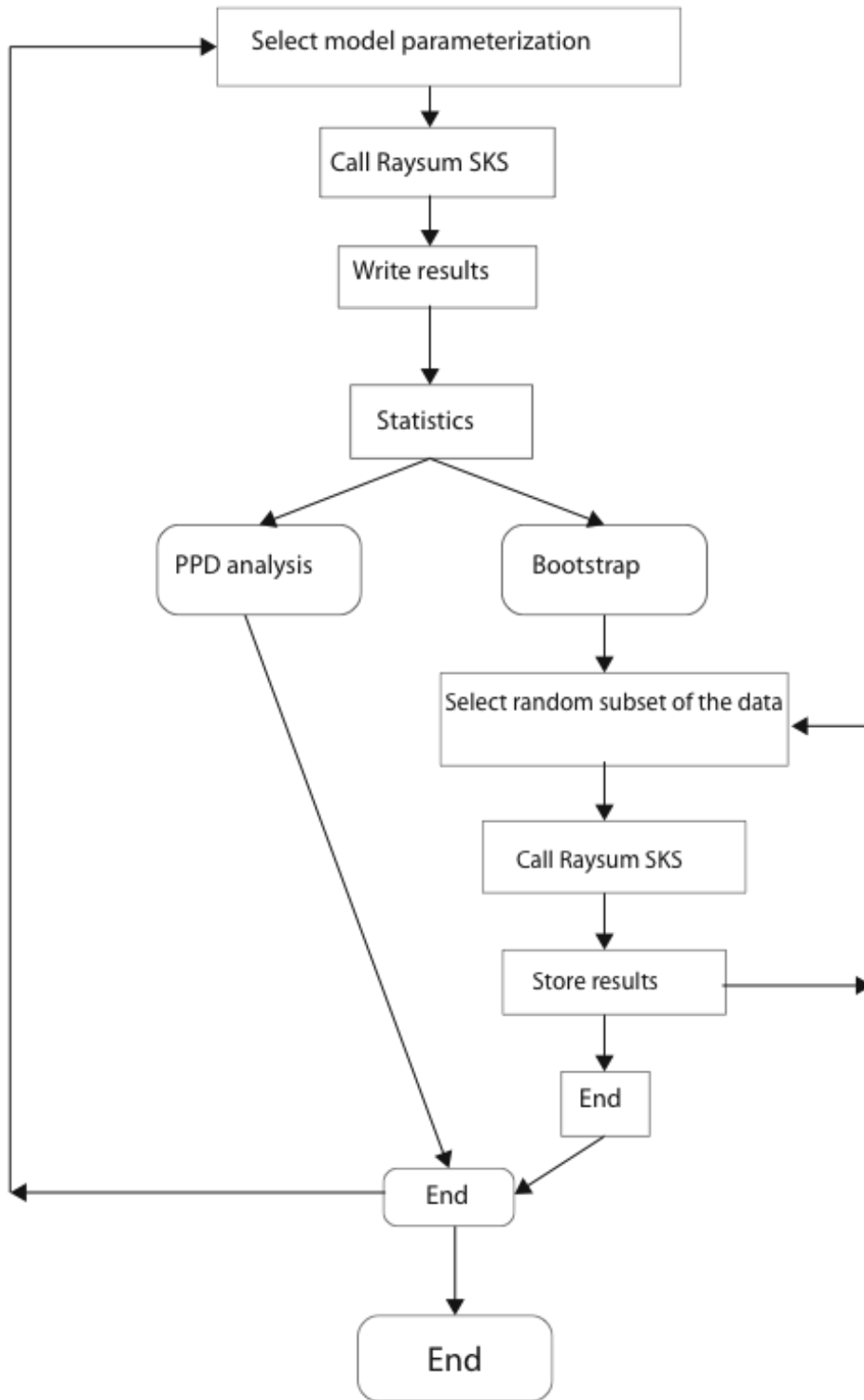


**Figure 33.** Processing stream for Raysum-SKS

The user then chooses whether to proceed with PDF assessment, or perform a bootstrap analysis. The PDF assessment uses a second Fortran program written by Huiyu Yuan, and based on one written by Malcolm Sambridge, to generate the posterior probability density function, which is then used to calculate the model expectation and the 1- and 2-D posterior probability density marginals that can be graphically displayed. The bootstrap function calls an iterative loop which randomly generates a subset of the data, calls Raysum\_SKS to find the best fitting solution, stores that solution, and repeats the process. The stored solutions can then be graphically plotted. The processing stream shown in **figure 32** is repeated for each model parameterization.

### ***3.1.4 Synthetic seismograms***

Synthetic seismograms are generated with a third Fortran program written by Huiyu Yuan, Seis-spread-response-sameni (seis-spread). The processing stream is shown in **figure 34**. The program allows the user to control both the event parameters (back-azimuth, incidence angle, and polarization), and well as the input anisotropic model. The program outputs a text file containing the radial, transverse, and vertical amplitude responses for each synthetic event, which is then read into Matlab. All traces are normalized by the root-mean-square amplitude of the particle motion, and randomly generated noise is added (see **figure 35**). Synthetic seismograms can be generated for any event geometry and any anisotropic model.

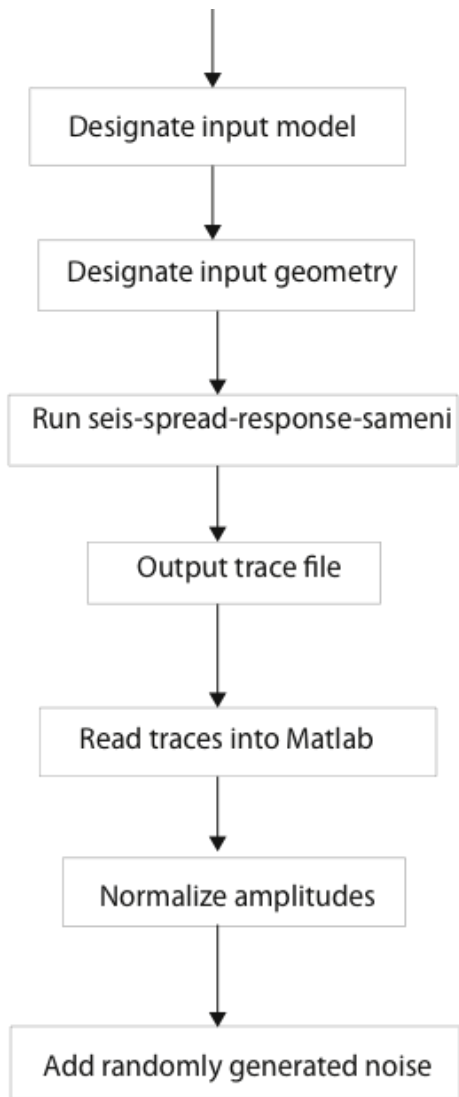


**Figure 34.** Processing stream for generating synthetic seismograms.

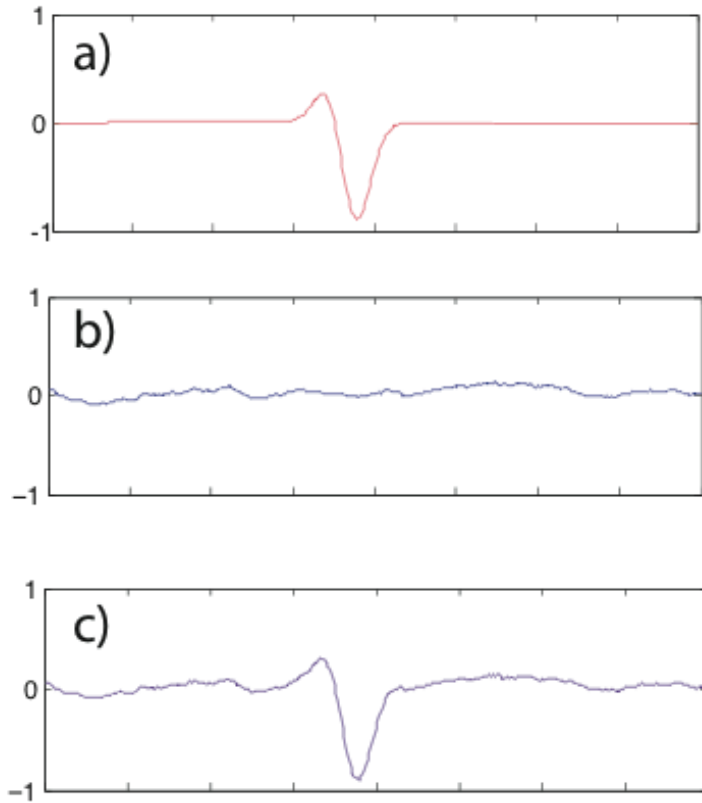


**Figure 35.** Adding noise to synthetics. **a)** Synthetic radial component output by seis-spread with amplitude normalized to 1. **b)** Example of randomly generated noise. **c)** Randomly generated noise in (b) added to synthetic seismogram in (a).

### ***3.1.5 Processing limitations and paths forward***

In its current state, the process used in this study is made less efficient by moving between Fortran and Matlab programs. In theory, Raysum\_SKS, the PDF program, and seis-spread can all be rewritten in Matlab, not only improving efficiency, but giving the user more control. However, time limitations of a Master's project didn't allow for this. Dr. Derek Schutt is currently working on writing the whole process into Matlab, with the eventual goal of integrating this method into the graphical user interface (GUI) SWS program SplitLab [Wüstefeld *et al.*, 2007], which provides the user with a manual, per-event approach that maintains user control during event selection, preprocessing, and SWS processing. A particular advantage of moving to Matlab will be to improve

the estimation of confidence bounds. Discussions with Dr. Jay Breidt have shown us that the chi-squared misfit estimation of Yuan et al., [2007], can be improved.

### **3.2 Recommendations for ongoing work**

The development of this method is an on going process. The basic framework is established, and we've shown with this study that this approach is cable of and necessary for expanding our scientific understanding of mantle deformation processes beneath continents. With the vast amount of broadband seismic data available for the North American continent, from permanent arrays, dense temporary arrays, and the EarthScope Transportable Array project, this approach could help to re-define our understanding of how continents formed. However, several objectives must be achieved before continent-wide scale analyses can begin.

In order to efficiently handle vast quantities of data, the processes of data selection, quality control, and splitting window selection need to be intelligently automated, or visual inspection needs to be reduced to a minimum. Currently, visual inspection is required to confirm proper window selection and weed out other inconsistencies that aren't accounted for via basic signal to noise filters. However, this process is both time consuming and subjective, and avenues for automation should be explored.

In discussions with Dr. Jay Breidt, we've found that the chi-squared errors associated with our SKS waveforms found via the method of *Yuan et al.* [2007] are partially incorrect due to the presence of an autocovariance in the signal. The improper calculation our waveform errors can propagate through to the model inference stage, thus affecting the PDF distributions from which we interpret our results. Dr. Breidt is currently working with us to remove all covariance from the signal in order to properly calculate our chi-squared values. Furthermore, we've learned that Raysum\_SKS runs into issues with precision, particularly when solving for dipping layers of

anisotropy. We are currently transitioning to a similar, but more precise algorithm called Anirec, that should give us more accuracy when modeling dipping layers.

Most importantly, it is vital that we fully understand and quantify the limitations of this method in resolving complex anisotropic structures. This can be achieved with an improved method for testing synthetic seismograms. Due to the time limitations of a Master's thesis, computational processing issues could not be fully resolved in order to do this, but all the required components are in place. Questions regarding the minimum back azimuthal coverage required to resolve complexity, acceptable noise levels, and uniqueness of solutions can all be addressed when future researchers are able to have full control over the synthetic testing process. Lastly, we are transitioning from using the Neighborhood Search Algorithm to employing a full grid search. Issues with control over the NA process have led us to seek alternative solutions to problems with computational energy needs.

## LITERATURE CITED

- Andsell, K. M. (2005), Tectonic evolution of the Manitoba-Saskatchewan segment of the Paleoproterozoic Trans Hudson Orogen, Canada, *Can. J. Earth Sci.*, 42, 741-759.
- Becker, T.W., J. B. Kellogg, G. Ekstrom, R. J. O'Connell 2003, Comparison of azimuthal seismic anisotropy from surface waves and finite strain from global mantle-circulation models. *Geophys. J. Int.*, 155, 696-714.
- Becker, T. W., S. Lebedev, and M. D. Long (2012), On the relationship between azimuthal anisotropy from shear wave splitting and surface wave tomography, *J. Geophys. Res.*, 117, B01306.
- Chevrot, S., and R. D. van der Hilst (2003), On the effects of a dipping axis of symmetry on shear wave splitting measurements in a transversely isotropic medium, *Geophys. J. Int.*, 152, 497–505.
- Courtier, A. M., J. B. Gaherty, J. Revenaugh, M. G. Bostock, and E. J. Garnero (2010), Seismic anisotropy associated with continental lithosphere accretion beneath the CANOE array, northwestern Canada, *Geology*, 38, 887-890.
- Crotwell, H. P., T. J. Owens, and J. Ritsema (1999), The TauP Toolkit: Flexible seismic travel-time and ray-path utilities, *Seis. Res. Let.*, 70, 154–160.
- Crampin, S. and J. H. Lovell (1991), A decade of shear-wave splitting in the Earth's crust: what does it mean? What use can we make of it? And what should we do next?, *Geophys. J. Int.*, 107, 387-407.
- Dahl, P. S., D. K. Holm, E. T. Gardner, F. A. Hubacker, and K. A. Foland (1999), New constraints on the timing of Early Proterozoic tectonism in the Black Hills (South Dakota), with implications for docking of the Wyoming province with Laurentia, *GSA Bulletin*, 111, 1335-1349.

- Davies, J. H., and F. vonBlackenburg (1995), Slab breakoff: A model of lithosphere detachment and its test in the magmatism and deformation of collisional orogens, *Earth and Planet Sci. Lett.*, 129, 85-102.
- Dewitt, E., J. A. Redden, A. B. Wilson, and D. Buscher (1986), Mineral resource potential and geology of the Black Hills National Forest, South Dakota and Wyoming, *U. S. Geol. Surv. Bull.*, 1580.
- Dziewonski, A. M., and D. L. Anderson (1981), Preliminary reference Earth model, *Phys. Earth Planet. Inter.*, 25, 297-356.
- Efron, B., and R. J. Tibshirani (1993), *An Introduction to the Bootstrap*, Chapman and Hall/CRC, Florida.
- Fouch, M., K. Fischer, E. Parmentier, M. Wyssession, and T. Clarke (2000), Shear wave splitting, continental keels, and patterns of mantle flow. *J. Geophys. Res.*, 105, 6255-6275.
- Fouch, M., and S. Rondenay (2006), Seismic anisotropy beneath stable continental interiors, *Phys. Earth Planet. Inter.*, 158, 292-320.
- Frederiksen, A. W., and M. G. Bostock (2000), Modelling teleseismic waves in dipping anisotropic structures, *Geophys. J. Int.*, 141, 401 - 412.
- Gaherty, J. B., and T. H. Jordan (1995), Lehmann Discontinuity as the base of an anisotropic layer beneath continents, *Sci.*, 268, 1468-1471.
- Goldstein, P., A. Snoke, (2005), "Sac Availability for the IRIS Community", Incorporated Institutions For Seismology Data Management Center Electronic Newsletter, <http://www.iris.edu/news/newsletter/vol7no1/page1.htm>.
- Goldstein, P., D. Dodge, M. Firpo, Lee Minner (2003), "SAC2000: Signal processing and analysis tools for seismologists and engineers", Invited contribution to "The IASPEI International Handbook of Earthquake and Engineering Seismology", Edited by WHK Lee, H. Kanamori, P.C. Jennings, and C. Kisslinger, Academic Press, London.

- Gorman, A. R., B. Nemeth, R. M. Clowes, and Z. Hajnal (2006), An investigation of upper mantle heterogeneity beneath the Archean and Proterozoic crust of western Canada from Lithoprobe controlled-source seismic experiments, *Tectonophys.*, 416, 187-207.
- Gosselin, D. C., J. J. Papike, R. E. Zartman, and Z. E. Peterman (1988), Archean rocks of the Black Hills, South Dakota: Reworked basement from the southern extension of the Trans-Hudson Orogen, *Geol. Soc. Am. Bull.*, 100, 1244-1259.
- Gripp, A. E., and R. G. Gordon (2002), Young tracks of hotspots and current plate velocities, *Geophys. J. Int.*, 150, 321-361.
- Hajnal, Z., K. M. Andsell, and K. E. Ashton (2005), Introduction to the special issue of Canadian Journal of Earth Sciences: The Trans-Hudson Orogen Transect of Lithoprobe, *Can. J. Earth Sci.*, 42, 379-383.
- Hammer, P. T. C., R. M. Clowes, F. A. Cook, K. Vasudevan, and A. J. van der Velden (2011), The big picture: A lithospheric cross section of the North American Continent, *GSA Today*, 21.
- Hoffman, P. F. (1989), Precambrian geology and tectonic history of North America, in *The Geology of North America - An Overview*, edited by A. W. Bally and A. R. Palmer, pp. 447 – 512, *Geology Society of America*, Boulder, CO.
- Iidaka, T., and F. Niu (2001), Mantle and crust anisotropy in the eastern China region inferred from waveform splitting of SKS and PpSms, *Earth and Planets Space*, 53, 159-168.
- Jenkins, G. M., and D. G. Watts (1968), *Spectral Analysis and its Applications*, Holden-Day, New York.
- Jung, H., and S. Karato (2001), Water-induced fabric transitions in olivine aggregates, *Sci.*, 293, 1460-1463.
- Kaminski, E. (2002), The influence of water on the development of lattice preferred orientations in olivine aggregates, *Geophys. Res. Lett.* 29, 1576.
- Karato, S. (1992), On the Lehmann discontinuity, *Geophys. Res. Lett.*, 19, 2255-2258.

- Karato, S., J. Haemyeong, I. Katayama, and P. Skemer (2008), Geodynamic significance of seismic anisotropy of the upper mantle: New insights from laboratory studies, *Annu. Rev. Earth Planet. Sci.*, 36, 59-95.
- Levin, V., and J. Park (1997), P-SH conversions in a flat-layered medium with anisotropy of arbitrary orientation, *Geophys. J. Int.*, 131, 253-266.
- Liu, H., P. M. David, and S. Gao (1995), SKS splitting beneath southern California, *Geophys. Res. Lett.*, 22, 767-770.
- Long, M. K., and P. G. Silver (2009), Shear wave splitting and mantle anisotropy: Measurements, interpretations, and new directions, *Surv. Geophys.*, 30, 407-461.
- Mainprice, D., and A. Nicolas (1989), Development of shape and lattice preferred orientations: application of the seismic anisotropy of the lower crust. *J. Of Structural Geology*, 1, 175-189.
- Menke, W., and V. Levin (2003), The cross-convolution method for interpreting SKS splitting observations, with application to one and two-layer anisotropic earth models, *Geophys. J. Int.*, 154, 379-392.
- Montagner, J., D. Griot-Pommeroy, and J. Lave (2000), How to relate body wave and surface wave anisotropy, *J. Geophys. Res.*, 105, 15-27.
- Nemeth, B., R. M. Clowes, and Z. Hajnal (2005), Lithospheric structure of the Trans-Hudson Orogen from seismic refraction- wide angle reflection studies, *Can. J. Earth Sci.*, 42, 435-456.
- Ozalaybey, S., and M. K. Savage (1995), Shear-wave splitting beneath Western United States in relation to plate tectonics, *J. Geophys. Res.*, 100, 135-149.
- Pysklywec, R. N., O. Gogus, J. Percival, A. R. Cruden, and C. Beaumont (2010), Insights from geodynamical modeling on possible fates of continental mantle lithosphere: collision, removal, and overturn, *Can. J. Earth Sci.*, 47, 541-563.
- Ribe, N. M. (1992), On the relationship between seismic anisotropy and finite strain, *J. Geophys. Res.*, 97, 8737-8747.

- Ringler, A. T., and C. R. Hutt (2010), Self-noise models of seismic instruments, *Seis. Res. Lett.*, 81, DOI: 10.1785/gsstl/81.6.972.
- Sambridge, M. (1999a), Geophysical Inversion with a Neighbourhood Algorithm -I. Searching a parameter space, *Geophys. J. Int.*, 138, 479 – 494.
- Sambridge, M. (1999b), Geophysical Inversion with a Neighbourhood Algorithm -II. Appraising the ensemble, *Geophys. J. Int.*, 138, 727 – 746.
- Sambridge, M., and K. Mosegaard (2002), Monte carlo methods in geophysical inverse problems, *Rev. Geophys.*, 40, DOI: 10.1029/2000RG000089.
- Savage, M. K. (1999), Seismic anisotropy and mantle deformation; What have we learned from shear wave splitting?, *Rev. Geophys.*, 37, 65–106.
- Savage, M. H., and A. F. Sheehan (2000), Seismic anisotropy and mantle flow from the Great Basin to the Great Plains, western United States, *J. Geophys. Res.*, 105, 715-734.
- Savage, M. K., and P. G. Silver (1993), Mantle deformation and tectonics: constraints from seismic anisotropy in the western United States, *Phys. Earth. Planet. Int.*, 78, 207-227.
- Schutt, D. L., and E. D. Humphreys (2001), Evidence for a deep asthenosphere beneath North America from western United States SKS splits, *Geology*, 29, 291-294.
- Silver, P.G. and S. Kaneshima (1993), Constraints on mantle anisotropy beneath Precambrian North America from transportable experiment, *Geophys. Res. Lett.*, 20, 1127-1130.
- Silver, P. G., and W. W. Chan (1988), Implications for continental structure and evolution from seismic anisotropy, *Nature*, 335, 34-39.
- Silver, P. G., and W. W. Chan (1991), Shear wave splitting and subcontinental mantle deformation, *J. Geophys. Res.*, 96, 429–416.
- Silver, P. G., and M. K. Savage (1994), The interpretation of shear-wave splitting parameters in the presence of two anisotropic layers, *Geophys. J. Int.*, 119, 949–963.

- Silver, P.G. (1996), Seismic anisotropy beneath the continents: probing the depth of geology, *Ann. Rev. Earth Planet. Sci.*, 24, 385-432.
- Silver, P. G., and M. D. Long (2010), The non-commutivity of shear wave splitting operators at low frequencies and implications for anisotropy tomography, *Geophys. J. Int.*, 184, 1415-1427.
- Snyder, D. and M. Bruneton (2007), Seismic anisotropy of the Slave craton, NW Canada, from joint interpretation of SKS and Rayleigh waves, *Geophys. J. Int.*, 169, 170-188.
- Streckeisen, G. (1987), Very-broad-band feedback seismometers, STS-1 V/VBB and STS-1 H/VBB Manual.
- Tian, Y., Y. Zhou, K. Sigloch, G. Nolet, and G. Laske (2011), Structure of North America constrained by simultaneous inversion of multiple-frequency *Sh*, *SS*, and Love waves, *J. Geophys. Res.*, 116, doi:10.1029/2010JB007704.
- Vinnik, L. P., L. I. Makeyeva, A. Milev, and A. Y. Usenko (1992), Global patterns of azimuthal anisotropy and deformations in the continental mantle, *Geophys. J. Int.*, 111, 433-447.
- White, D. J., M. D. Thomas, A. G. Jones, J. Hope, B. Nemeth, and Z. Hajnal (2003), Geophysical transect across a Paleoproterozoic continent-continent collision zone: The Trans Hudson Orogen, *Can. J. Earth Sci.*, 42, 384-402.
- Whitmeyer, S. J., and K. E. Karlstrom (2007), Tectonic model for the Proterozoic growth of North America, *Geosphere*, 3, 220-259.
- Wüstefeld, A., G.H.R. Bokelmann, C. Zarole, and G. Barruol (2007), SplitLab - A Shear wave splitting environment in Matlab, *Computers & Geosciences*, DOI:10.1016/j.cageo.2006.
- Yuan, H. B. K. and B. Romanowicz (2010), Lithospheric layering in the North American craton, *Nature*, 466, 1063-1069.
- Yuan, H., B. K. Romanowicz, M. Fischer, and D. Abt (2011), 3-D shear wave radially and azimuthally anisotropic velocity model of the North American upper mantle. *Geophys. J. Int.*, 184: 1237-1260.

- Yuan, H., K. Dueker, and D. L. Schutt (2007), Testing five of the simplest upper mantle anisotropic velocity parameterizations using teleseismic S and SKS data from the Billings, Montana PASCAL array, *J. Geophys. Res.*, 113, doi:10.1029/2007JB005092.
- Zang, S. Q., and S. Karato (1995), Lattice preferred orientation of olivine aggregates deformed in simple shear, *Nature*, 375, 774-777.

## APPENDICIES

### APPENDIX A: Sod Recipe in xml format

```
<?xml version="1.0"?>
<sod>
<eventArm>
  <eventFinder>
    <name>IRIS_EventDC</name>
    <dns>edu/iris/dmc</dns>
    <originTimeRange>
      <startTime>1997-01-01T00:00:00.000Z</startTime>
      <endTime>2001-01-01T00:00:00.000Z</endTime>
    </originTimeRange>
    <magnitudeRange>
      <min>6.0</min>
      <max>10</max>
    </magnitudeRange>
  </eventFinder>
  <removeEventDuplicate>
    <timeVariance>
      <unit>HOUR</unit>
      <value>1</value>
    </timeVariance>
  </removeEventDuplicate>
  <printlineEventProcess>
    <template>
      $event.getLongitude('##0.0000;-##0.0000') $event.getLatitude('##0.0000;-##0.0000') $event.getDepth('###0.##') ${event.getTime('yyyy_DDD_HH_mm_sss')}
      $event.magnitudeValue$event.magnitudeType
    </template>
  </printlineEventProcess>
</eventArm>
<networkArm>
  <networkFinder>
    <name>IRIS_NetworkDC</name>
    <dns>edu/iris/dmc</dns>
  </networkFinder>
  <stationAND>
    <stationArea>
      <boxArea>
        <latitudeRange>
          <min>36</min>
          <max>45</max>
        </latitudeRange>
        <longitudeRange>
          <min>-113</min>
          <max>-103</max>
        </longitudeRange>
      </boxArea>
    </stationArea>
  </stationAND>
</networkArm>
</sod>
```

```

        </longitudeRange>
    </boxArea>
</stationArea>
</stationAND>
<bandCode>B</bandCode>

    <gainCode>H</gainCode>
</networkArm>
<waveformVectorArm>
    <distanceRange>
        <unit>DEGREE</unit>
        <min>85</min>
        <max>135</max>
    </distanceRange>
    <phaseRequest>
        <model>prem</model>
        <beginPhase>SKS</beginPhase>
        <beginOffset>
            <unit>SECOND</unit>
            <value>-90</value>
        </beginOffset>
        <endPhase>SKS</endPhase>
        <endOffset>
            <unit>SECOND</unit>
            <value>+90</value>
        </endOffset>
    </phaseRequest>
    <fixedDataCenter>
        <name>IRIS_PondDataCenter</name>
        <dns>edu/iris/dmc</dns>
    </fixedDataCenter>
    <printlineSeismogramProcess/>
    <responseGain/>
    <rMean/>
    <rTrend/>
    <phaseCut>
        <model>prem</model>
        <beginPhase>SKS</beginPhase>
        <beginOffset>
            <unit>SECOND</unit>
            <value>-50</value>
        </beginOffset>
        <endPhase>SKS</endPhase>
        <endOffset>
            <unit>SECOND</unit>
            <value>+50</value>
        </endOffset>
    </phaseCut>
    <threeComponentData/>
    <vectorTrim/>

```

```

<rotateGCP/>
<ORWaveformProcessWrapper>
  <seismogramAND>
    <embeddedEventChannelProcessor>
      <embeddedChannel>
        <orientationCode>R</orientationCode>
      </embeddedChannel>
    </embeddedEventChannelProcessor>
    <phaseSignalToNoise>
      <phaseName>SKS</phaseName>
      <shortOffsetBegin>
        <unit>SECOND</unit>
        <value>-5</value>
      </shortOffsetBegin>
      <shortOffsetEnd>
        <unit>SECOND</unit>
        <value>10</value>
      </shortOffsetEnd>
      <longOffsetBegin>
        <unit>SECOND</unit>
        <value>-20</value>
      </longOffsetBegin>
      <longOffsetEnd>
        <unit>SECOND</unit>
        <value>-5</value>
      </longOffsetEnd>
      <ratio>3</ratio>
    </phaseSignalToNoise>
  </seismogramAND>
</ORWaveformProcessWrapper>
<sacWriter>

```

```

<location>${station.code}/${event.filizedTime}/${station.code}.${channel.code}.sac</location>
  <phaseTimeHeader>
    <model>prem</model>
    <phaseName>SKS</phaseName>
    <tHeader>0</tHeader>
  </phaseTimeHeader>
  <phaseTimeHeader>
    <model>prem</model>
    <phaseName>S</phaseName>
    <tHeader>1</tHeader>
  </phaseTimeHeader>
  <phaseTimeHeader>
    <model>prem</model>
    <phaseName>ScS</phaseName>
    <tHeader>2</tHeader>
  </phaseTimeHeader>
  <phaseTimeHeader>
    <model>prem</model>

```

```
        <phaseName>SKKS</phaseName>
        <tHeader>3</tHeader>
    </phaseTimeHeader>
    <phaseTimeHeader>
    <model>prem</model>
        <phaseName>SKiKS</phaseName>
        <tHeader>4</tHeader>
    </phaseTimeHeader>
    <phaseTimeHeader>
    <model>prem</model>
        <phaseName>SKIKS</phaseName>
        <tHeader>5</tHeader>
    </phaseTimeHeader>
    <phaseTimeHeader>
    <model>prem</model>
        <phaseName>Sdiff</phaseName>
        <tHeader>6</tHeader>
    </phaseTimeHeader>
</sacWriter>
</waveformVectorArm>
</sod>
```